Photoacoustics 2 (2014) 87–101

Contents lists available at ScienceDirect

Photoacoustics

journal homepage: www.elsevier.com/locate/pacs

Review Article

# Sensitivity of photoacoustic microscopy

Junjie Yao, Lihong V. Wang *

*Optical Imaging Laboratory, Department of Biomedical Engineering, Washington University in St. Louis, St. Louis, MO 63130, USA*

ARTICLE INFO

*Article history:*
Received 5 March 2014
Accepted 12 April 2014
Available online 24 April 2014

*Keywords:*
Photoacoustic microscopy
Detection sensitivity
Absorption contrast
Ultrasonic transducer
Early cancer detection
Contrast agents

ABSTRACT

Building on its high spatial resolution, deep penetration depth and excellent image contrast, 3D photoacoustic microscopy (PAM) has grown tremendously since its first publication in 2005. Integrating optical excitation and acoustic detection, PAM has broken through both the optical diffusion and optical diffraction limits. PAM has 100% relative sensitivity to optical absorption (i.e., a given percentage change in the optical absorption coefficient yields the same percentage change in the photoacoustic amplitude), and its ultimate detection sensitivity is limited only by thermal noise. Focusing on the engineering aspects of PAM, this Review discusses the detection sensitivity of PAM, compares the detection efficiency of different PAM designs, and summarizes the imaging performance of various endogenous and exogenous contrast agents. It then describes representative PAM applications with high detection sensitivity, and outlines paths to further improvement.



**Contents**



## 1. Introduction

In the last decade, photoacoustic tomography (PAT) has been drawing increasing attention from various research communities, including imaging, chemistry, material, physics, and biomedicine [1–3]. Briefly, in PAT, as photons travel in tissue, some of them are

* Corresponding author.
*E-mail address:* lhwang@wustl.edu (L.V. Wang).

http://dx.doi.org/10.1016/j.pacs.2014.04.002

absorbed by molecules and their energy is partially or completely converted into heat. The heat then induces an initial pressure rise, which propagates as an acoustic wave. An ultrasonic transducer or transducer array detects the acoustic wave to form an image, which maps the original optical energy deposition in the tissue [4].

As shown in Fig. 1, PAT can be classified according to system attributes. These attributes include the image formation method, spatial resolution, number of ultrasonic transducer elements, image contrast, probe size, and image dimensions. For example, PAT has two major implementations based on their image formation methods [5]: reconstruction-based photoacoustic computed tomography (PACT), and acoustic-lens-based photoacoustic imaging. In PACT, the object is excited by a broadened laser beam. Ultrasonic transducers are placed around the object to simultaneously receive the ultrasonic waves emitted. At any given time point, an ultrasonic transducer integrates initial photoacoustic pressures over a spherical surface centered at the detector with a radius equal to the product of the speed of sound and the time. This integration is referred to as the spherical Radon transform. The spherical Radon transform can then be inverted by various reconstruction methods [6], such as the universal back-projection method [7] and iteration-based time reversal method [8], to map the laser-induced initial pressure rise distribution, which reflects the optical absorption contrast in the object.

Instead of reconstructing an image digitally in PACT, a focused ultrasound transducer is used for analog image reconstruction, most commonly, in photoacoustic microscopy (PAM). Upon a pulsed laser excitation, the focused ultrasound transducer picks up a time-resolved PA signal emitted from the acoustic focal zone. A single laser pulse yields a 1D image. Scanning across the tissue yields a 2D image. Raster scanning yields a 3D image. The acoustic focusing can be accomplished either by affixing an acoustic lens (spherical or cylindrical) to a flat ultrasonic transducer or by curving the active ultrasonic element itself. Here, we define PAM as an implementation of PAT with a spatial resolution finer than 50 μm, since the naked eye can discern features larger than 50 μm. By using a 5 MHz focused ultrasonic transducer, deep-penetration photoacoustic macroscopy (PAMac) relaxes the lateral resolution to 560 μm and extends the maximum imaging depth to a few centimeters. PAMac is not classified as microscopy but is covered in this Review to demonstrate the scalability of PAT. In addition, photoacoustic endoscopy (PAE) is considered as a variant of PAM for internal organ imaging, which is typically rotational scanning based.

Harnessing the rich optical absorption contrast and the low ultrasonic scattering in tissue, PAT is one of the fastest growing biomedical imaging modalities [1]. Comprehensive reviews of PAT technology can be found in previous publications [3,9]. Here, we will focus only on the development of PAM technology. PAM typically employs raster-scanning of its optical and acoustic foci and forms images directly from acquired depth-resolved signals [10]. While the axial resolution of PAM is primarily determined by the imaging depth and the frequency response of the ultrasonic transducer, its lateral resolution is determined by the product of the point spread functions of the dual foci. Based on its configuration, PAM can be further classified into optical-resolution PAM (OR-PAM), where the optical focus is much smaller than acoustic focus [11], and acoustic-resolution PAM (AR-PAM), where the acoustic focusing is tighter [12,13].

Among all the imaging parameters of PAM, detection sensitivity is of particular interest, since it reflects the minimum number of targets at different length scales (e.g., melanoma tumor cells, hepatitis virus, glioblastoma-targeting nanoparticles and hemoglobin molecules) needed to measure signals above the noise and provide accurate diagnosis of disease [10,14–17]. For example, in early cancer detection, it is required that PAM should be able to detect as few as $10^4$ cancer cells (0.01 mg or 0.01 mL), because malignant switching in cancer progression typically needs $\sim 10^5$ cells growing as a single mass [18]. In PAM, energy is transformed through three steps. First, optical (electromagnetic) energy is

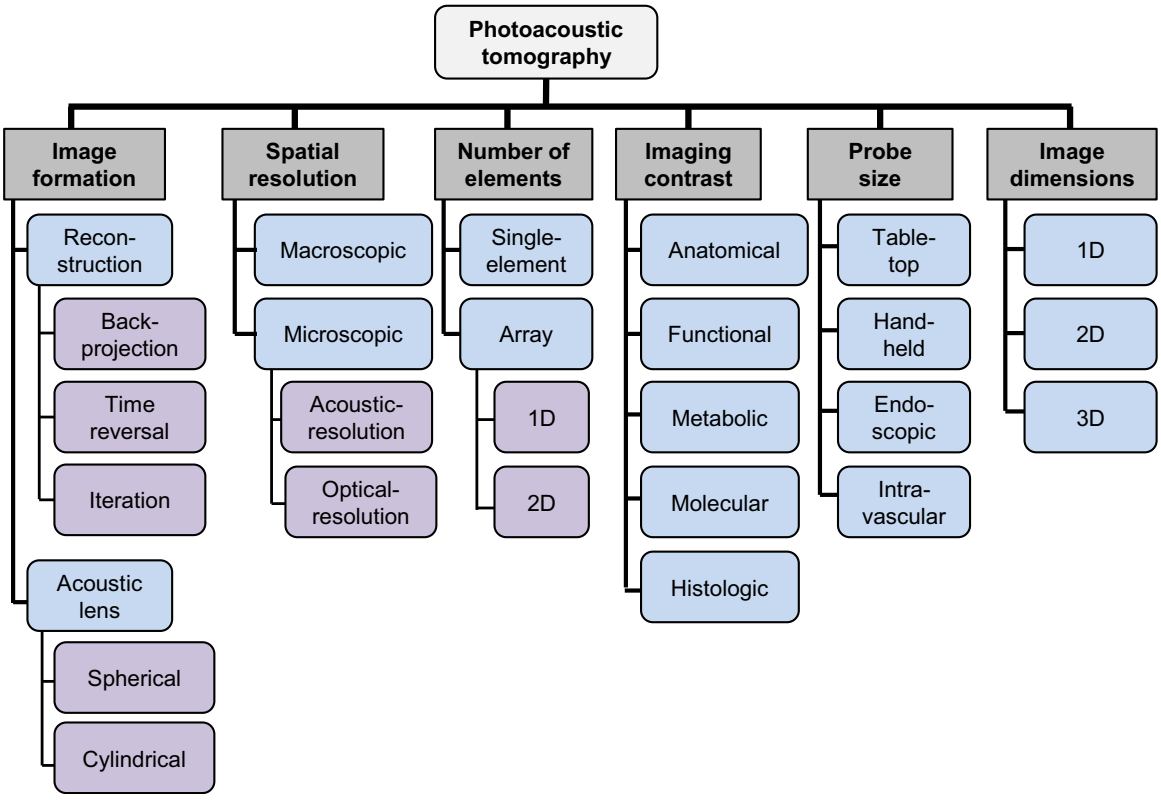


**Fig. 1.** Classification of photoacoustic tomography based on different system attributes.

transformed to thermal energy via absorption and nonradiative relaxation. Then, thermal energy is transformed to mechanical energy through thermoelastic expansion. Finally, mechanical energy is transformed to electrical energy via piezoelectric effect by ultrasonic transducers [1,19,20]. In each step, the energy conversion efficiency is limited while noise is present. Therefore, the detection sensitivity of PAM is affected by a number of factors, such as the incident laser fluence, optical absorption coefficient of the target, and detection efficiency of the ultrasonic transducer. With optimal illumination and detection configurations, the detection sensitivity of PAM is fundamentally limited by thermal noise, which can present in the acoustic detection system as well as in the medium itself [15].

In this Review, we will first analyze the signal and noise generation in PAM, and discuss the fundamental detection sensitivity that PAM can achieve. Then, we will compare the current engineering solutions designed to maximize the detection sensitivity of PAM. Endogenous and exogenous contrast agents for high-sensitivity PAM imaging will also be discussed through representative biomedical applications. At last, possible paths toward further improvement in PAM detection sensitivity will be outlined.

## 2. Photoacoustic signal generation

In PAM, PA signals can be generated by either pulsed excitation [11,12] or intensity-modulated continuous-wave (CW) excitation [15,21–24]. Although CW lasers are generally less expensive, pulsed lasers are much more frequently used in PAM, mainly because the PA signal-to-noise ratio (SNR) in pulsed excitation is greater than that in CW excitation [21,22] if the same number of photons are delivered or ANSI safety limits are observed [25].

### 2.1. Fundamentals of photoacoustic signal generation

When thermal confinement is satisfied, we obtain the PA equation for an arbitrary absorbing target with an arbitrary excitation source [4]:

$$\left(\nabla^2 - \frac{1}{v_s^2}\frac{\partial^2}{\partial t^2}\right) p(\vec{r},t) = -\frac{\beta}{C_P}\frac{\partial H(\vec{r},t)}{\partial t}, \tag{1}$$

where $p(\vec{r},t)$ denotes the acoustic pressure rise at location $\vec{r}$ and time $t$, $v_s$ is the speed of sound (~1480 m/s in water), $\beta$ denotes the thermal coefficient of volume expansion ($\sim 4\times10^{-4}\,\mathrm{K}^{-1}$ for muscle), $C_p$ denotes the specific heat capacity at a constant pressure (~4000 J/kg/K for muscle), and $H(\vec{r},t)$ is the heating function. The left hand side of Eq. (1) describes wave propagation in an inviscid medium, whereas the right-hand side represents the source. Eq. (1) shows that the propagation of a PA pressure wave is driven by the first time derivative of the heating function $H(\vec{r},t)$. Therefore, time-invariant heating does not generate a PA pressure wave; only time-variant heating does.

In the case of a delta-pulse excitation, the initial pressure rise in the target is related to the heating function by

$$p_0 = \Gamma H = \Gamma\eta_{th}\mu_a F, \tag{2}$$

where $p_0$ is the initial pressure rise, and $\Gamma$ is the Grueneisen parameter defined as $\Gamma = \beta v_s^2/C_P$, $\eta_{th}$ is the percentage of absorbed energy that is converted to heat, $\mu_a$ is the optical absorption coefficient, and $F$ is the optical fluence. PA response to a finite-duration pulsed or CW excitation can be computed by convolving the heating function with the impulse response solution to Eq. (1), based on the Green's function approach [4].

The intensity of an excitation pulse is often approximated by a Gaussian function as

$$I_{pulsed}(t) = \frac{F}{\tau\sqrt{2\pi}}\exp\left(-\frac{t^2}{2\tau^2}\right), \tag{3}$$

where $F$ is the fluence per pulse, and the full width at half maximum (FWHM) of the temporal pulse profile is $2\sqrt{2\ln 2}\tau$.

For a point target, the resultant PA pressure is proportional to the time derivative of the excitation pulse. We have the maximum PA pressure as

$$p_{pulsed,\max} \propto \frac{\Gamma\eta_{th}\mu_a F}{\tau^2}. \tag{4}$$

In the case of intensity-modulated CW excitation, the light intensity is given by

$$I_{CW}(t) = I_0[1+\sin(w_c t)], \tag{5}$$

where $I_0$ is the time-averaged light intensity, and $w_c$ is the modulation frequency. Then, the maximum PA pressure from a point target is given by

$$p_{CW,\max} \propto \Gamma\eta_{th}\mu_a w_c I_0. \tag{6}$$

Comparing Eqs. (4) and (6), we can see that pulsed excitation is more efficient in generating PA signals. According to the ANSI standard, in the visible spectral region on the skin surface, the maximum permitted $F$ is 20 mJ/cm$^2$ and the maximum permitted $I_0$ is 200 mW/cm$^2$ [25]. At such ANSI limits, for example, if the pulse width is 10 ns for pulsed excitation and the modulation frequency is 50 MHz for CW excitation, $p_{pulsed,\max}$ is approximately six orders of magnitude (~120 dB) stronger than $p_{CW,\max}$. If the number of incident photons is conserved, $p_{pulsed,\max}$ is approximately seven orders of magnitude (~140 dB) stronger than $p_{CW,\max}$.

In addition, unlike single-frequency CW excitation, pulsed excitation can provide axial resolution: the acoustic flight time in pulsed excitation provides depth information about the absorbing targets, and the axial resolution is jointly determined by the laser pulse width, frequency-dependent acoustic attenuation of the tissue, and detection bandwidth of the ultrasonic transducer. By contrast, single-frequency CW excitation cannot separate signal contributions from absorbers at different depths [22], unless chirped modulation or other wide-band techniques are used [21].

### 2.2. Optimize PA signal generation

Maximizing PA signal generation is critical for improving the detection sensitivity of PAM. Several factors can be optimized to improve the PA signal generation.

The absorption coefficient $\mu_a$ describes the probability of photon energy absorption in a medium per unit infinitesimal path length, and is heavily wavelength dependent. In a medium containing many absorbers of the same kind with number density of $N_a$ and absorption cross section of $\sigma_a$, the absorption coefficient $\mu_a$ is given by $\mu_a = N_a\sigma_a$. Increasing the detection sensitivity naturally requires the use of absorbers with high $\sigma_a$. Larger molecules generally have greater absorption cross sections with some exceptions. For example, nanoparticles with surface plasmon resonance have larger absorption cross sections than most organic dye molecules [26].

Nevertheless, as $\mu_a$ increases, the increase in PA signal tends to saturate when the mean absorption length (i.e., $1/\mu_a$) is comparable to or smaller than the axial resolution, a phenomenon called the spatial saturation effect, where the spatial decay of specific optical absorption (i.e., absorbed optical energy per unit volume) cannot be resolved [27]. As $\mu_a$ increases further, the increased PA signal component falls into higher frequencies. After low-pass filtering by acoustic propagation in tissue, the PA signal

strength in the detectable bandwidth does not change. In this case, the detected PA signal relies on only the incident optical energy regardless of the optical absorption coefficient [28].

The thermal conversion efficiency $\eta_{th}$ reflects the percentage of absorbed photon energy that is converted into heat. The PA effect relies on the nonradiative relaxation of excited molecules to the ground state. Therefore, minimizing radiative relaxation, such as fluorescence and phosphorescence, increases the PA signal generation. Chromophores with zero or low fluorescence quantum yield, such as hemoglobin and melanin, are commonly used as PA imaging contrast. Recently, Förster resonance energy transfer (FRET) has been demonstrated in PAM imaging. In FRET PAM, the reduction of donor fluorescence emission (e.g., Rhodamine 6G), as a result of nonradiative energy transfer to the acceptor (e.g., DQOCI), results in an increase in PA emissions from the donors [29].

The Grueneisen parameter $\Gamma$ is a dimensionless factor that reflects the conversion efficiency from thermal energy (heat) to mechanic energy (pressure). At body temperature (37 °C), $\Gamma$ of water or high-water-content tissue is about 0.2, so, for each milliKelvin temperature rise, an 8-mbar (800 Pa) pressure rise is produced. $\Gamma$ itself is temperature dependent [4]. Specifically, around body temperature, every degree increase in temperature results in a 5% increase in $\beta$, a 0.1% increase in $v_s$ and a 0.02% increase in $C_P$. Therefore, an increase in the equilibrium temperature in the medium results in an increase in $\Gamma$, and thus the PA signal amplitude (~5% per °C). This temperature dependence has been used for temperature sensing with PAM [30,31]. As discussed later, theoretically speaking, an increase in equilibrium temperature also results in an increase in acoustic thermal noise in the medium. However, at body temperature, every degree increase in temperature results in only a 0.15% increase in thermal noise amplitude, which is negligible. Note that, here we refer to the equilibrium temperature of the medium, not the change in temperature of the absorbing target due to the laser heating. In linear PA generation, the instantaneous temperature increase in the target due to the laser pulse heating is on the order of millikelvins, and its effect on the Grueneisen parameter is negligible. In nonlinear PA generation, the initial deposition of heat at the beginning of the excitation pulse increases the thermal expansion coefficient, and thus the generation of subsequent PA signal by the continuing addition of heat takes place with higher efficiency [32]. This effect is called PA thermal nonlinearity.

In linear PAM, the PA wave pressure is proportional to the fluence $F$. To optimize PA detection sensitivity, using the maximum permitted $F$ is logically the most appealing and usually the most effective solution. Nevertheless, potential laser damage to biological tissue is a concern when high laser fluence is used. ANSI has detailed laser safety standards with regard to tissue types and illumination conditions [25]. Generally speaking, laser fluence under the ANSI limit is required for safety. However, in PA imaging with nanosecond excitation, signal generation shares the same mechanism as tissue damage, which is related to the photothermal process. This suggests that excitation fluence above the ANSI limit can be justified for weakly absorbing targets, since a weak PA signal is accompanied by a low chance of thermal damage. This is different from femtosecond excitation used in two-photon microscopy, where optical breakdown is the dominant damage mechanism [33].

As in any optical excitation technique, photoacoustic generation also exhibits nonlinearity to excitation intensity. On one hand, optical absorption saturation prevents the pressure amplitude from increasing indefinitely with optical intensity [34,35]. On the other hand, thermal nonlinearity can offset optical absorption saturation to some extent, as it typically enhances photoacoustic generation [32]. Furthermore, at very high optical intensities, heat can generate strong shock waves through cavitation, which may cause tissue damages [36].

In optical absorption saturation, $I_{sat} = h\nu/(\sigma_a \tau_r)$ is the saturation intensity, where $h$ is the Planck's constant, $\nu$ is the optical frequency, and $\tau_r$ is the absorption relaxation time of the molecule. As the excitation intensity approaches $I_{sat}$, the generated PA signal increases with significant nonlinearity until it approximately approaches a finite value. In optical thermal nonlinearity, the absorbed optical energy induces an increase in the local temperature, which elevates the generated PA pressure. Combining the optical saturation with the thermal nonlinearity, the effective optical fluence can be approximated by

$$F_{eff} \approx \frac{F}{1 + I/I_{sat}} \left(1 + k_{th} \frac{F}{1 + I/I_{sat}}\right), \tag{7}$$

where $k_{th}$ is a proportionality constant that describes the heating efficiency of the local temperature by the absorbed optical energy. $k_{th}$ is a compound parameter that is highly sensitive to the volume in which heat is deposited and to the rate at which heat diffuses [32].

The practical impact of Eq. (7) needs to be carefully considered. The thermal nonlinear effect is due to heat accumulation in the absorber-medium complex, while the saturation effect is due to the depletion of ground-state molecules in the target. When the optical fluence is low, both the saturation and thermal nonlinearities can be neglected, and thus $F_{eff} \approx F$. As the optical fluence increases, the two nonlinear effects compete with each other as determined by the physical properties of both the absorbers and the medium. It is worth noting that, by providing the PA signal with nonlinear dependence on the optical fluence, both of the nonlinear effects can be used for sub-diffraction PA imaging (i.e., PAM with a lateral resolution finer than the optical-diffraction limit).

The excitation pulse width is also important in optimizing PA signal generation. Simply speaking, the excitation pulse width should be chosen according to the targeted detection bandwidth. In PAM, the stress confinement on the axial direction requires a pulse width to be less than the acoustic transit time across the resolution voxel (typically on the scale of nanoseconds). The excitation pulse width can affect the axial and lateral resolutions of AR-PAM, and the axial resolution of OR-PAM. In addition, the pulse width is related to the generated PA signal amplitude at the target. As shown in Fig. 2, when the stress confinement is not satisfied, i.e., the excitation pulse is long compared with the stress confinement, the resultant PA pressure at the target is roughly inversely proportional to the square of the pulse width [32]. In this sense, a shorter pulse is more efficient in generating PA signals than a longer pulse. However the increased PA signal mostly falls into the high frequency region. As we know, after the low-pass filtering by tissue, high frequency acoustic components will not be picked up by the ultrasonic transducer, similar to the spatial saturation effect discussed above [37,38]. As can be seen from Fig. 2, once the stress confinement is satisfied, the excitation pulse can be approximated as a delta function, and the resultant PA pressure at the transducer surface relies only on the excitation pulse energy, and is not sensitive to the pulse width anymore [39]. Therefore, it is not necessary to further reduce the pulse width once the targeted signal bandwidth is matched. The pulse width needs to be optimized according to the desired spatial resolution or imaging depth. Furthermore, because excitation intensity is pulse width related, pulse width also affects PA signal generation through the absorption saturation effect [35].

## 3. Noise in photoacoustic imaging

Noise is the fundamental limitation on PAM detection of single molecules [15,16]. In PAM, noise mainly arises from three sources: thermal acoustic noise from the medium, thermal noise from the

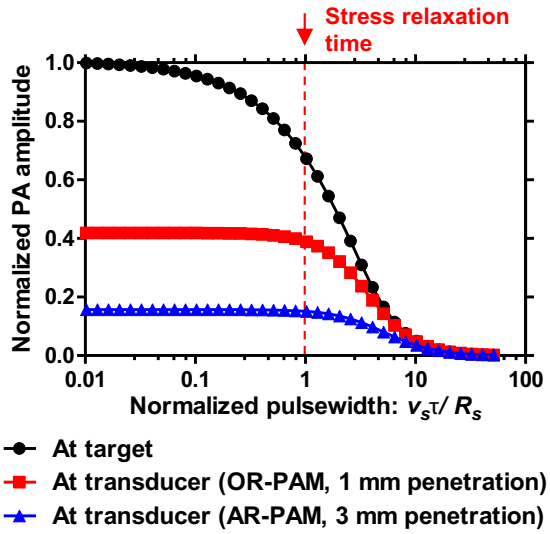


**Fig. 2.** Simulated maximum PA pressure amplitude at the target and at the ultrasonic transducer surface as a function of the excitation pulse width in OR-PAM and AR-PAM. The excitation pulse width is normalized by the stress relaxation time, while the pulse energy is a constant. The PA amplitude of all curves is normalized by the maximum PA amplitude at the target (black curve). $R_s$ is the axial resolution. The target is 6 mm from the transducer. In OR-PAM, the target is 1 mm under the tissue surface [48], while in AR-PAM the target is 3 mm under the tissue surface [12]. Acoustic attenuation coefficient in water: $2.5 \times 10^{-14}\,\mathrm{Hz^{-2}\,m^{-1}}$. Acoustic attenuation coefficient in soft tissue: $2.5 \times 10^{-12}\,\mathrm{Hz^{-1.2}\,m^{-1}}$.

ultrasonic transducer, and electronic noise from the amplifier. The power spectral density (PSD) of thermal acoustic noise detected by the ultrasonic transducer, which describes the distribution of noise power per unit bandwidth as a function of frequency, is given by [15]

$$N_a(f) = \eta_d(f) k_B T, \tag{8}$$

where $\eta_d(f)$ is the transducer efficiency at frequency $f$, defined as the fraction of acoustic power converted to electrical power; $k_B$ is the Boltzmann constant ($1.38 \times 10^{-23}$ J/K); and $T$ is the absolute temperature of the medium in Kelvin.

An ultrasonic transducer also generates its own noise, which can be modeled as Johnson noise [15]. When the transducer has an internal resistance matched to the load resistance of its amplifier, the power spectral density of the thermal noise generated by the transducer is given by [15]

$$N_d(f) = k_B T. \tag{9}$$

Finally, the electronic noise generated by the amplifier is given by [15]

$$N_{am}(f) = N_d(f)[F_n - 1], \tag{10}$$

where $F_n$ denotes the noise factor of the amplifier and has a typical value of 2 over its bandwidth.

Summing the above three noise sources gives the total noise power in PAM as

$$P_{noise} = \int_{\Delta f} d f [\eta_d(f) + F_n] k_B T, \tag{11}$$

where $\Delta f$ is the detection bandwidth of the ultrasonic transducer. Low-frequency narrow-band ultrasonic transducers made of piezoceramics such as PZT-5 can readily achieve an efficiency $\eta_d$ of 0.5 or better. In this case, the noise contributions from the medium and transducer are within the same order of magnitude. By contrast, high-frequency broadband transducers made of piezopolymers such as PVDF typically have an efficiency $\eta_d$ of 0.001–0.01; hence, the ultrasonic transducer noise dominates.

To decrease the thermal noise in the medium, one might attempt to chill the medium. However, while the noise amplitude decreases as the square root of the temperature, the PA signal amplitude drops much faster due to the linearly reduced thermal expansion coefficient. At room temperature, a one degree temperature drop results in a 0.2% decrease in the noise amplitude and a 5% decrease in the PA signal amplitude. Therefore, the chilling method is counter-effective. Certainly, noise can be reduced by performing signal averaging, at the expense of imaging speed. Alternatively, a noise reduction solution is to decrease the detection bandwidth of the ultrasonic transducer and its associated electronics [16]. For example, in CW excitation mode, a narrow-band resonant ultrasonic transducer can be used with a lock-in amplifier, and thus a detection bandwidth of ~1 Hz can be readily achieved [15]. This translates into a 1000 times reduction in noise amplitude, compared with its counterpart in pulsed excitation with a detection bandwidth of tens of megahertz. However, as discussed above, because the pulsed excitation is much more efficient in generating PA signals than the CW excitation, the SNR by pulsed excitation is still higher than that by the CW excitation on the condition that the same number of photons are delivered or ANSI safety limits are observed [22]. In addition, since the axial resolution of PAM can be approximately estimated as $R_a \approx 0.88 v_s/\Delta f$, a narrow detection bandwidth results in a degraded axial resolution [10,40].

## 4. Ultimate detection sensitivity in PAM

In biomedical imaging, the most widely used parameter to quantify detection sensitivity is the noise-equivalent concentration (NEC) or the noise-equivalent number of molecules per resolution voxel (NEN). The latter is the product of the former and the resolution voxel volume. In PAM, a few other quantities can also be used for quantifying the detection sensitivity, including noise-equivalent optical absorption coefficient ($NE\mu_a$) and noise-equivalent pressure rise (NEP). These quantities are highly interconnected but emphasize different aspects of the imaging system. In our study of the ultimate detection sensitivity, we will begin by considering NEP.

NEP is defined as the photoacoustic pressure at the target that generates a transducer output equal to the noise amplitude. For an ultrasonic transducer with a center frequency of $f_0$ and a detection bandwidth $\Delta f$, if we assume that the detector efficiency is uniform such that $\eta(f) \approx \eta(f_0)$, we have [15]

$$NEP \approx \frac{\sqrt{k_B T \Delta f [1 + F_n/\eta(f_0)] Z_a}}{e^{-\alpha f_0^2 L} N A_A / 2}. \tag{12}$$

$Z_a$ denotes the characteristic acoustic impedance of the medium (~$1.5 \times 10^6$Rayls for water); $L$ is the focal length of the transducer; $\alpha$ denotes the acoustic attenuation coefficient in units of $\mathrm{Hz^{-2}\,m^{-1}}$; and $NA_A$ is the numerical aperture of the acoustic lens.

The numerator of Eq. (12) is in fact the NEP at the transducer surface [15], while the denominator denotes the acoustic loss during propagation from the target to the transducer surface. As can be seen, NEP increases with $\Delta f$, and decreases with $L$ and $NA_A$. Here, as an example, we will estimate the detection sensitivity of the sub-wavelength photoacoustic microscopy (SW-PAM) developed by Zhang et al. [41]. For the spherically focused piezoelectric transducer with a bandwidth of 50 MHz, a focal length of 6 mm, and a detector area of ~30 $\mathrm{mm^2}$ at room temperature, the NEP is ~77 Pa.

For a single molecule with an optical absorption cross section of $\sigma_a$, if the molecule is much less than the acoustic wavelength, the

generated PA pressure $p_s$ can be expressed as [15,32]

$$p_s(r) = \frac{\eta_{th} F \sigma_a \beta}{4\pi\tau^2 C_p r}, \tag{13}$$

where $r$ is the distance from the molecule to the point of measurement.

Combining Eqs. (12) and (13), we can estimate the number of molecules required to generate PA pressure equal to NEP, referred to as the noise equivalent number of molecules (NEN).

$$NEN = NEP \times \frac{4\pi\tau^2 C_p}{\eta_{th} F e^{-\mu_t' L} \sigma_a \beta}, \tag{14}$$

where $\mu_t'$ denotes the optical transport interaction coefficient of tissue. As can be seen, NEN decreases with $F$ and $\sigma_a$. For nonfluorescent chromophores such as hemoglobin and melanin, $\eta_{th} \approx 1$. In SW-PAM, with the ANSI permitted surface fluence of 20 mJ/cm$^2$ at 532 nm,the estimated NAN of oxy-hemoglobin is $\sim 1.6 \times 10^4$. It needs to be mentioned that the light attenuation in tissue is neglected in SW-PAM, which may result in an underestimation of NEN.

Then, we can quantify the noise-equivalent concentration NEC as

$$NEC = \frac{NEN}{V_R}, \tag{15}$$

and the noise-equivalent absorption coefficient $NE\mu_a$ as

$$NE\mu_a = NEC \times \xi_a, \tag{16}$$

where $V_R$ denotes the spatial resolution volume, and $\xi_a$ is the molar extinction coefficient of the absorbing molecules. In SW-PAM, an NEN of $1.6 \times 10^4$ oxy-hemoglobin molecules corresponds to an NEC of ~38 nM and an $NE\mu_a$ of $\sim 1.5 \times 10^{-3}$ cm$^{-1}$.

All the above quantities are highly scalable. With regard to different quantities, the ultimate detection sensitivity can be achieved by optimizing corresponding imaging and/or molecule properties. In particular, there is a trade-off between NEC and spatial resolution. Relaxing the spatial resolution can improve NEC, and vice versa. NEC is further limited by the permitted maximum excitation fluence at the tissue surface and the optical attenuation in tissue [4]. Of course, the safety standards are lower than the damage thresholds. Therefore, it might be justifiable to use laser exposure above the ANSI limits but below the damage thresholds in some applications. In addition, NEC is highly target and wavelength dependent. NEC can be enhanced by using contrast agents with high absorption coefficients. For example, it has been reported that PEGylated nanoshells have an absorption cross-section at 800 nm that is $6.5 \times 10^5$ times as large as that of hemoglobin at 532 nm [42].

## 5. High-sensitivity PAM systems

Biological systems need to be studied on both macroscopic and microscopic scales. By adjusting the excitation and detection configurations, all of the key imaging parameters of PAM, including spatial resolution, imaging depth and detection sensitivity, can be scaled over a wide range with the same optical absorption contrast. Such high scalability is critical for comprehensive study of biological phenomena over different length scales, and for the translation of laboratory discovery to clinical practice. Comprehensive details about PAM characterizations and biomedical applications can be found in previous Review articles [1,10], and a summary of the scalable imaging performance of representative PAM systems is shown in Fig. 3. To achieve the ultimate detection sensitivity, PAM needs to optimize its optical illumination and acoustic detection, based on the desired imaging specifications.

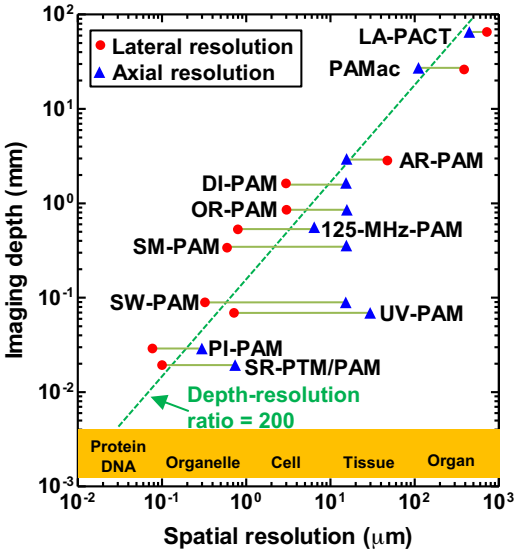


**Fig. 3.** Imaging depth versus spatial resolution in multi-scale photoacoustic tomography. The red circles denote lateral resolution, and the blue squares denote axial resolution. AR-PAM, acoustic resolution photoacoustic microscopy (PAM)[12]; DI-PAM, double-illumination PAM [113]; LA-PACT, linear-array PA computed tomography [135]; OR-PAM, optical resolution PAM [11]; 125-MHz-PAM, PAM with a 125 MHz ultrasonic transducer [40]; PAMac, deep photoacoustic macroscopy [136]; PI-PAM, photo-imprint PAM [137]; SR-PTM/PAM, super-resolution photothermal/photo acoustic microscopy [87]; SM-PAM, submicronPAM [138]; SW-PAM, subwavelength PAM [41]; UV-PAM, ultraviolet PAM [64].

### 5.1. Optimal optical excitation in PAM

The major goal of optical design in PAM is to maximize the delivered optical fluence to the target, especially at depths beyond the optical diffusion limit. In fact, the major difference between OR-PAM and AR-PAM lies in the optical excitation configuration. In OR-PAM, the laser beam is tightly focused to a diameter ranging from sub-micrometer to a few micrometers. The acoustic detection area is generally more than 100 times larger than the optical excitation area. By contrast, in AR-PAM, the laser beam is only loosely focused with a diameter of a few millimeters in the optical quasi-diffusion regime. Due to the weak optical focusing and the strong optical scattering, the optical excitation area is much wider than the acoustic detection zone. Therefore, in terms of laser energy usage, OR-PAM is at least two orders of magnitude more efficient than AR-PAM. While AR-PAM typically requires an excitation pulse energy on the level of tens of millijoules, OR-PAM needs only a few hundred nanojoules. Therefore, the light delivery in OR-PAM is generally not a concern. However, when the imaging depth goes deeper than the optical diffusion limit, optical focusing becomes so inefficient that OR-PAM gradually transits into AR-PAM [43,44]. Here, we will mainly discuss optimal light delivery in AR-PAM.

Although AR-PAM relies on diffuse photon absorption for imaging deep targets, there exist optimal illumination schemes that most efficiently deliver photons to the targets and result in the best detection sensitivity [45]. In AR-PAM, two illumination patterns have been explored: bright-field illumination and dark-field illumination. Compared with dark-field illumination, bright-field illumination is more efficient in delivering optical energy to shallow depths, due to the relatively short photon path length and small excitation beam spot [46]. However, Monte Carlo simulations show that, when the desired imaging depth is beyond 2 mm in bright-field illumination, the optical fluence at the tissue surface is at least 10 times higher than that at the targeted depth. It might be challenging to delivery enough photons to the targeted depth

without causing thermal damage to the tissue surface. By contrast, in dark-field illumination, a ring-shape illumination pattern is coaxially aligned with the focused ultrasonic transducer [12,13]. Compared with bright-field illumination, the large illumination area in dark-field reduces the difference between the optical fluence at the tissue surface and deep region, and reduces the otherwise strong interference of the extraneous PA signal from the superficial area.

In dark-field AR-PAM, the ring shape illumination can be formed by the combination of a spherical conical lens and a weakly focusing optical condenser. By changing the inner radius and the incident angle of the illumination laser beam, its geometric focal depth can be adjusted. However, due to the strong optical scattering in tissue, the highest optical fluence region, referred as the effective optical focus, is generally shallower than the geometrical optical focus. The effective optical focus should ideally overlap with the ultrasonic focus, which, however, is challenging when the targeted imaging depth is more than 1 mm. In dark-field AR-PAM, Monte Carlo simulations have been used to study the influence of two parameters, the inner radius and the incident angle, on the optical fluence and the effective optical focus [45,47]. The depth of the effective optical focus increases with the inner radius of the dark field, suggesting that a larger dark field is required to image a deeper target.

There are some other considerations in the optical design in PAM. Compared with free-space light delivery, fiber-based light delivery is less efficient and limited by the fiber coupling efficiency and the damage threshold of the optical fiber [11,48]. However, fiber-based light delivery is preferred in high-speed PAM systems due to its ease of routing [48,49]. While multi-mode fiber or fiber bundle is used in AR-PAM for maximum light delivery [12,50,51], single-mode fiber is needed in OR-PAM for optimal focusing capability [43,48].

### 5.2. Optimal acoustic detection in PAM

The importance of optimal acoustic detection in PAM can never be over emphasized. So far, piezoelectric ultrasonic transducers [16] and optical-acoustic detectors [52–56] have been used to detect the wide-band acoustic waves in PAM. Optical interferometers, such as a Fabry-Perot ultrasound sensor, have several advantages over conventional piezoelectric transducers: (1) the all-optical detection eliminates the water environment required for acoustic propagation, although the optical sensor is still in acoustic contact with the tissue surface; (2) the transparent nature of the optical sensors reduces the engineering difficulty for the combination of PAM with other optical imaging modalities; and (3) the optical sensors are relatively easy to miniaturize for PA endoscopy. However, optical sensors are typically less sensitive than piezoelectric detectors. For example, an NEP of 8 Pa has been achieved by a Fabry-Perot (FP) ultrasound sensor over a 20 MHz bandwidth, while an NEP of 0.13 Pa has been achieved by a piezoceramic transducer with a similar bandwidth and a diameter of 6 mm [15,57,58]. However, the sensitivity of a piezoelectric detector falls off with decreasing element size, whereas the sensitivity of an optical sensor is largely independent of the element size. Below a certain breaking-even point in element size, the optical sensor provides higher sensitivity. This breaking-even point depends on a variety of factors such as the NEP of the optical sensor and the material of the piezoelectric detector as well as the bandwidth. As an approximate estimation, given the NEPs of FP sensors and PVDF detectors reported in the literature, it appears that the breaking-even point lies at a diameter of 1 mm for a bandwidth of 20 MHz [59]. Nevertheless, because of the ease of fabrication and high sensitivity, piezoelectric detectors are more frequently used in PAM systems.

For ultrasonic detectors, detection sensitivity trades off with detection bandwidth. Resonant ultrasonic detectors with a narrow bandwidth are the most sensitive. However, unless working in CW excitation mode, PAM generally uses wideband ultrasonic detectors to accommodate the PA signals generated by pulsed excitation. Therefore, it is logical to choose acoustic detectors that best match the bandwidth of generated PA signals. Four piezoelectric materials are commonly used for wideband ultrasound detection in PAM: lithium niobate, quartz, PVDF and PZT-5 [16,38]. Among them, lithium niobate and quartz have the lowest sensitivity, but they are easy to polish and thus widely used for detecting ultrasonic signals above 30 MHz. PZT-5 detectors have the best sensitivity, but have very high acoustic absorption above 20 MHz, and thus are typically used for relatively low frequency ultrasound detection. PVDF has a moderate sensitivity, in between lithium niobate/quartz and PZT-5. Because it has a similar acoustic impendence ($\sim 2.5 \times 10^6$ Rayls) to biological tissue ($\sim 1.5 \times 10^6$ Rayls), PVDF detectors have the lowest acoustic reflective loss at the detector surface. Recently, novel piezo-composite materials, e.g., PZT-epoxy composite, have been developed to provide greater detection sensitivity and bandwidth than the traditional piezoelectric materials [16].

### 5.3. Optical-acoustic combination in PAM

Unlike pure optical or ultrasound imaging, where the same optical or acoustic pathway can be shared by both excitation and detection, PAM needs to combine its optical excitation and acoustic detection. On one hand, the fact that excitation and detection have different energy formats naturally eliminates the leakage of the excitation signal into the detection system. On the other hand, it increases the engineering complexity of optical-acoustic combination for optimal detection sensitivity.

Generally speaking, in AR-PAM, the optical-acoustic combination favors the maximum delivery of photon energy, while in OR-PAM, the optical-acoustic combination favors the most efficient detection of the acoustic energy. In AR-PAM, because the laser beam is only weakly focused and there is virtually no limitation on the optical working distance, the spherically focused ultrasonic transducer is directly positioned coaxially with the illumination beam. Except for the acoustic transmission loss during propagation, there is basically no additional acoustic loss in this optical-acoustic combination.

In OR-PAM, because the laser beam is tightly focused and the optical objective lens has a limited working distance, the focused ultrasonic transducer cannot be directly positioned underneath the lens without blocking the optical focusing. To achieve confocal alignment of the optical and acoustic beams, transmission-mode and reflection-mode OR-PAM systems have been developed. In transmission-mode OR-PAM [41,60,61], the objective and ultrasonic transducer are on opposite sides of the sample. Typically, the ultrasonic transducer is on top of the sample for water coupling. This configuration is straightforward and presents little difficulty in the optical-acoustic combination, even for optical objectives with a high numerical aperture (NA). However, transmission-mode OR-PAM is greatly limited: it can image only thin samples, and is thus not suitable for many in vivo applications. By contrast, in reflection-mode OR-PAM, the optical objective and ultrasonic transducer are both on top of the sample. While reflection-mode OR-PAM is not limited by the sample thickness, its implementation is more complicated, making it difficult to realize a large NA in both optical illumination (for high spatial resolution) and ultrasonic detection (for high sensitivity) [62]. Further, when wide-range optical wavelengths are required in OR-PAM imaging, it can be difficult to maintain the optical-acoustic confocal alignment due to the severe chromatic aberration of the objective lens [63].

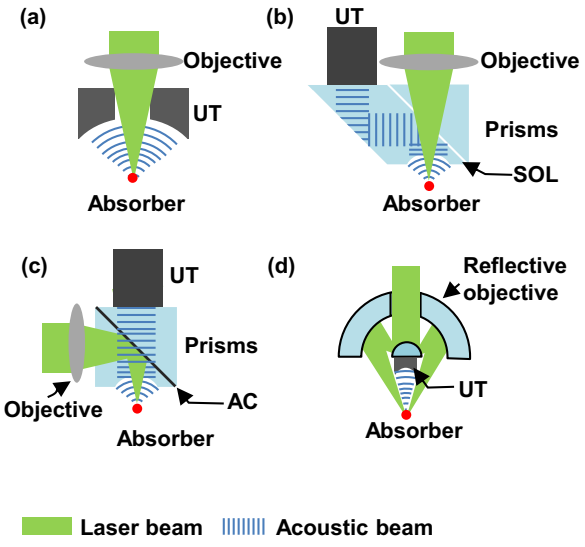


**Fig. 4.** Optical-acoustic combinations in OR-PAM. (a) A ring shape ultrasonic transducer (UT) is used with a central hole to pass the focusing laser beam [64]. (b) An optical-acoustic combiner is made of two prisms sandwiching a thin layer of silicone oil (SOL) [11]. The SOL is transmissive to the laser beam but reflective to the acoustic beam. (c) An optical-acoustic combiner is made of two prisms sandwiching a 100 nm thick aluminum coating (AC) layer [49]. The AC layer is transmissive to the acoustic beam but reflective to the laser beam. (d) An optically reflective objective is used to form a dark-centered illumination pattern, and a focused ultrasonic transducer is placed right beneath the objective [63].

So far, three methods have been explored for optical-acoustic combination in reflection-mode OR-PAM. The first method uses a customized ring-shape focused ultrasonic transducer, which has a central hole to pass the focused optical beam (Fig. 4a) [44,64]. The ultrasonic transducer is coaxially aligned with the objective lens to a common focus. A derivation of this design is to use a customized parabolic mirror with a conical hole to focus and redirect the ultrasonic waves [62]. Because of the central hole, the acoustic focusing is degraded and there is at least ~10% acoustic energy loss. The most significant drawback of this design is that these ring-shape transducers are not commercially available and thus have very limited choices. The second method uses a customized optical-acoustic combiner to redirect the optical or acoustic beam (Fig. 4b). In this design, a silicone oil layer sandwiched by two prisms, which is optically transparent but acoustically reflective, is used to achieve the confocal and coaxial alignment of the optical and acoustic beams [11,48]. Alternatively, a thin aluminum coating (~100 nm thick) between two prisms, which is optically reflective but acoustically transparent, can be used (Fig. 4c) [49,65]. The acoustic energy loss inside the combiner is negligible. However, this design is typically too big to be used with high NA objectives due to their short working distances. Another drawback is that only a flat transducer attached to an acoustic lens can be used. The acoustic impedance mismatch between the acoustic lens (glass: $\sim 12.1 \times 10^6$ Rayls) and water causes a 30% acoustic energy loss. The third method uses a reflective dark-field optical objective (Fig. 4d) [63]. Due to the long working distance of the reflective dark-field objective (>20 mm), a commercial focused ultrasonic transducer can be placed directly underneath the objective. The objective and the ultrasonic transducer are aligned coaxially and confocally for maximum sensitivity. This design can achieve a large NA in both optical illumination (NA: 0.6) and ultrasonic detection (NA: 0.5). Moreover, an impedance matching layer (1/4 wavelength thick) can be coated to the ultrasonic transducer surface, and thus the acoustic energy loss due to reflection will be reduced. Multiple matching layers can be used to further improve the acoustic transmission, though the optimization is considerably more complex [38]. In addition, unlike a refractive based objective, the reflective objective can cover a wide wavelength range without degrading the optical-acoustic confocal alignment.

There are several reported optical-acoustic combination designs in PAM which have gained other benefits at the cost of detection sensitivity. Off-axis PAM seeks to simplify the optical-acoustic alignment by placing a commercial ultrasonic transducer off-axis to the excitation laser beam [66]. Signals generated in the overlap of the illumination and detection zones are detected, providing the additional benefit of quasi-dark-field detection. However, this design has a very limited acoustic NA (<0.2) and thus suffers from low detection sensitivity. In addition, this design degrades the axial resolution, e.g., two times degradation at 60° off axis. Fabry-Perot ultrasound detectors are also used in OR-PAM [58]. The Fabry-Perot film is transparent for the excitation laser beam but reflective for the interrogation CW laser beam, so the excitation and detection can be easily configured in reflection-mode. However, as discussed above, the detection sensitivity of the Fabry-Perot detector is weaker than that of a commercial piezoelectric transducer.

## 6. Contrast agents for PAM

Both endogenous and exogenous contrast agents have been explored by high-sensitivity PA imaging. In biomedical studies, the advantages of endogenous contrast agents are undeniable. They are nontoxic and do not perturb the original tissue microenvironment; moreover, they are usually abundant in tissue and do not require costly and time-consuming regulatory approval. The most commonly imaged endogenous contrast agents in PAM can be classified into two categories, based on their primary absorbing wavelengths: (1) in the ultraviolet (UV) (180–400 nm) and visible (400–700 nm) regions, the primary absorbers for PA imaging include DNA/RNA [64,67], cytochrome *c* [60,68], bilirubin [69], myoglobin [60], hemoglobin [3] and melanin [70]; and (2) in the near-infrared region (700–1400 nm), lipid [41,71,72], water [73] and glucose [74] are the major absorbers for PA imaging. Fig. 5 summarizes the absorption spectra of common endogenous contrasts imaged by PAM. Among them, hemoglobin is most commonly used for PA vascular imaging in the visible wavelength region, where the imaging contrast between blood vessels and background tissues is more than 100. An NEC of 0.38 μM and an NEN of 0.27 zeptomol of hemoglobin (~160 molecules) have been experimentally demonstrated by sub-wavelength OR-PAM [41]. The detection sensitivity of hemoglobin by representative PAM systems is quantified using in vivo data reported in the literature (Fig. 6). It shows that detection sensitivity (NEN) increases with the imaging depth, another scalability of PAM.

Exogenous contrast agents have two advantages over endogenous ones [2,75]. First, the chemical and optical properties of exogenous contrast agents can be specifically engineered for maximum detection sensitivity. Second, exogenous contrast agents can be conjugated with targeting molecules (e.g., antibodies) to selectively bind to disease-specific cell surface receptors. So far, microbubbles, organic dyes, nanoparticles, and reporter gene proteins have been used as PAM contrast agents, enabling chemical, molecular and genetic imaging. To achieve deep penetration and avoid background absorption (e.g., by hemoglobin and water), most of these exogenous contrasts work in the red or near-infrared spectral regions. Among them, nanoparticles have been most widely used as PAM imaging contrasts due to their excellent optical absorbing capabilities and variety of sizes, shapes and compositions [2]. A low NEN of seven nanotubes has been reported with a laser fluence of 100 mJ/cm$^2$ at 900 nm [76]. In particular, because of their inert chemical properties, gold nanoparticles have been extensively investigated for tumor targeting [77–80], cortical vasculature

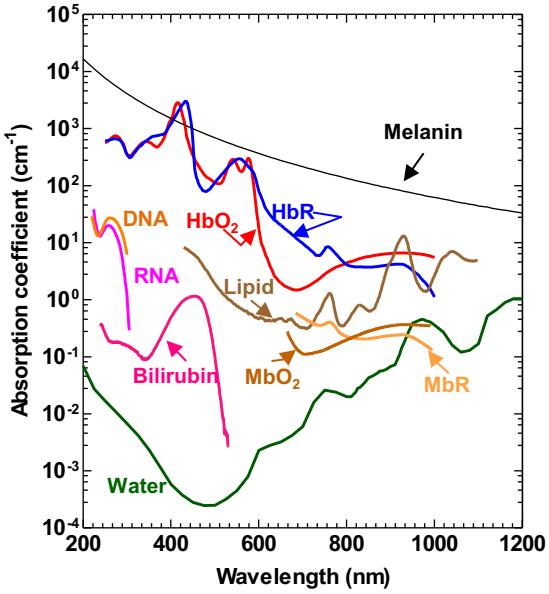


**Fig. 5.** Absorption spectra of major endogenous contrast agents in biological tissue at normal concentrations. Oxy-hemoglobin ($HbO_2$) and deoxy-hemoglobin (HbR), 150 g/L in blood; lipid, 20% by volume in tissue; water, 80% by volume in tissue; DNA and RNA, 1 g/L in cell nuclei; melanin, 14.3 g/L in medium human skin; reduced myoglobin (MbR) and oxy-myoglobin ($MbO_2$), 0.5% by mass in skeletal muscle; bilirubin, 12 mg/L in blood.
Reprinted with permission from [10].

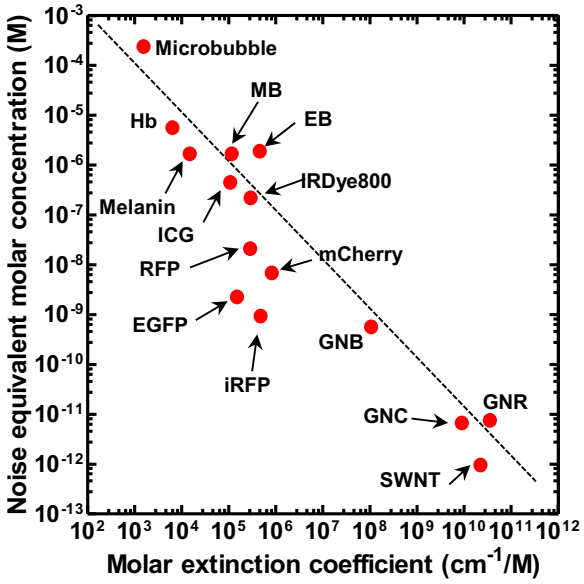


**Fig. 7.** Reported noise equivalent molar concentrations (NEC) of major endogenous and exogenous contrast agents, versus their molar extinction coefficients. Due to the lack of complete information, the incident fluence is not corrected here. EB, evens blue [139]; EGFP, enhanced green fluorescent protein [17]; GNB, gold nanobeacon [140]; GNC, gold nanocage [83]; GNR, gold nanorod [141]; Hb, hemoglobin [10]; ICG, indocyanine green [142]; IRDye800, near-infrared Dye800 [2]; iRFP, near-infrared red fluorescent protein [143]; MB, methylene blue [144]; mCherry, monomeric cherry protein [17]; Melanin, [145]; Microbubble, [146]; RFP, red fluorescent protein [143]; SWNT, single walled nanotube [76]. The dashed curve is power function fitting $y = 0.1x^{-1}$, where $y$ denotes NEC in molars and $x$ denotes the molar extinction coefficient in $cm^{-1}/M$. Note that $xy = 0.1$ $cm^{-1}$, which is the noise-equivalent absorption coefficient ($NE\mu_a$) at depths > 3 mm.

enhancement [81] and sentinel lymph node mapping [82–84]. Notably, due to the strong absorbing, single nanoparticle detection has been achieved by using OR-PAM with diffraction-limited or sub-diffraction-limited resolution [41,85–87].

Because of their dramatically different optical absorbing properties, the reported detection sensitivity (NEC) for exogenous contrast agents varies from millimolar to picomolar. Roughly, the reported NEC is on the level of millimolar for microbubbles, micromolar for organic dyes, picomolar for nanoparticles, and nanomolar for fluorescent proteins [10]. Fig. 7 summarizes the reported PAM detection sensitivity (NEC) of representative endogenous and exogenous contrast agents.

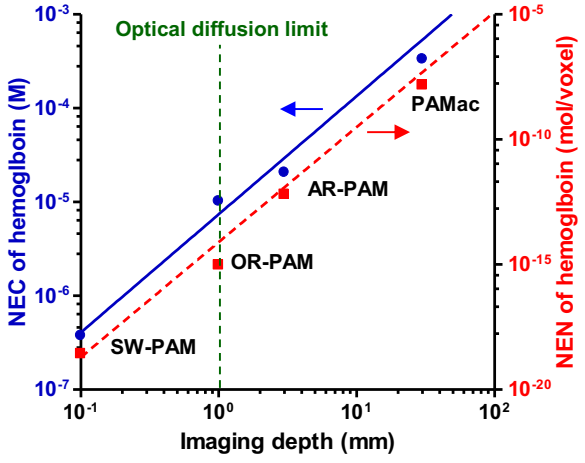


**Fig. 6.** Noise-equivalent molar concentration (NEC, blue circles) and noise-equivalent number (NEN, red squares) of hemoglobin molecules versus the imaging depth of different photoacoustic imaging systems. The results were quantified from the reported in vivo data in the literature. For a fair comparison, the incident fluence of each system is scaled to the ANSI limit for the skin at 570 nm (20 $mJ/cm^2$ at the skin surface) [10]. The blue solid curve is power function fitting of NEC $y = 7.4 \times 10^{-6}x^{1.3}$, where $y$ denotes NEC in molars and $x$ denotes the depth in mm. The red dashed curve is power function fitting of NEN $y = 7.8 \times 10^{-15}x^{4.6}$, where $y$ denotes NEN in moles and $x$ denotes the depth in mm.
Adapted with permission from [10].

## 7. High-sensitivity imaging and sensing by PAM

By offering high-resolution images with unique optical contrast, PAM has so far been applied to numerous preclinical and clinical studies, including vascular biology [88–90], oncology [42,70,91–95], neurology [96–99], ophthalmology [100–104], dermatology [105–109], gastroenterology [110–114], and cardiology [41,115–117]. In the interest of brevity, only a few representative applications that have demonstrated high detection sensitivity are highlighted in this Review. Information about more PAM applications can be found in recent Review articles [2,9,118,119].

### 7.1. Label-free single-cell photoacoustic flowoxigraphy

With high detection sensitivity, OR-PAM is capable of studying biological processes on the single cell level. Recently, by integrating fine spatial and temporal scales, PA flowoxigraphy, a new implementation of OR-PAM, has demonstrated multi-parametric imaging of oxygen release from single red blood cells (RBCs) in vivo (Fig. 8) [65]. By fast line scanning (20 Hz) along a capillary with two wavelength excitations, PA flowoxigraphy can simultaneously measure multiple hemodynamic parameters that are required to quantify the oxygen release rate by RBCs. Experimental results show that PA flowoxigraphy can be used to image the coupling between neural activity and oxygen delivery in response to different physiological challenges, which can be useful in understanding how the brain is powered at the single cell level.

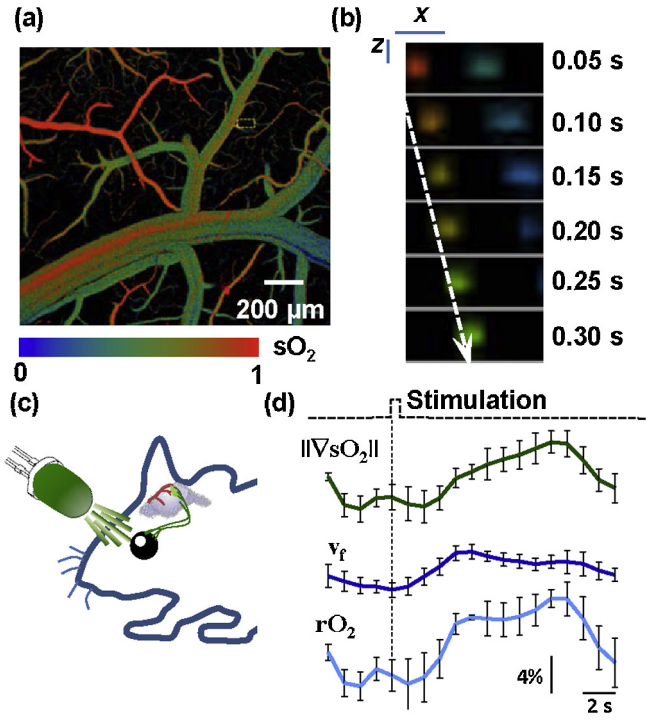


**Fig. 8.** Single cell label-free photoacoustic flowoxigraphy in vivo. (a) Oxygen saturation ($sO_2$) mapping of the brain vasculature. (b) Single cell oxygen unloading measurement was performed by fast line scanning along a capillary with two wavelength excitations. Blood flows from left to right. The dashed arrow follows the trajectory of a single flowing RBC. Scale bar: $x$ = 10 μm, $z$ = 30 μm. (c) Schematic of the experimental setup for imaging neuron-single-RBC coupling in the mouse visual cortex. The eye of a mouse was stimulated by a flashing LED. (d) Transient responses to a single visual stimulation. Clear increases were observed in the magnitude of the $sO_2$ gradient ($||\nabla sO_2||$), blood flow speed ($v_f$) and oxygen unloading rate ($rO_2$).
Reprinted with permission from [65].

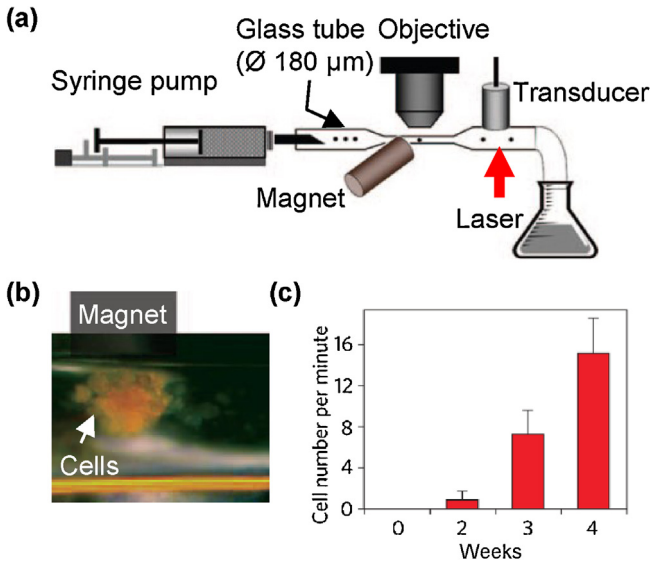


**Fig. 9.** Magnetically enhanced photoacoustic detection of circulating tumor cells. (a) In vitro testing setup for magnetically enhanced trapping of tumor cells. Magnetic-nanoparticle labeled tumor cells were flowing in a plastic tube at 0.5 mm/s. (b) Optical image of the tumor cells trapped by the magnet. (c) The increasing average rate of circulating tumor cells (CTCs) in a vein of a tumor-bearing mouse ear over a period of several weeks after the tumor inoculation, detected by magnetic enhanced photoacoustic microscopy.
Reprinted with permission from [78].

### 7.2. Photoacoustic detection of circulating tumor cells

Circulating tumor cells (CTCs) have been regarded as a potential predictor for metastasis, a hallmark of tumor malignancy [120]. However, due to the limited CTCs in the early stage cancer, blood-test-based ex vivo examination of CTCs is very challenging since it requires a large blood sample. Alternatively, on-site photoacoustic cytometry can be used to image the CTCs without drawing blood [78]. For example, taking advantage of the strong optical absorption of melanin at the near infrared wavelength, label-free photoacoustic cytometry has been used to detect circulating melanoma cells (CMCs) in the blood stream with a detection sensitivity of 1 CMC/mL blood on a 50 μm vessel [121]. This detection sensitivity can be improved by imaging a larger blood vessel. By using targeting magnetic-enriched nanoparticles, *in vivo* CTC detection has been demonstrated with a sensitivity of a few CTCs in whole human blood (~5 L), which makes it possible for early cancer detection (Fig. 9) [78]. Once detected, the captured CTCs can be microsurgically extracted for molecular and genetic tests or can be noninvasively ablated by therapeutic laser to prevent metastasis.

### 7.3. Nanotube enhanced tumor targeting by PAM

Early cancer diagnosis requires that PAM detects a small tumor with as few as $10^4$ tumor cells [18]. However, in most non-pigmented tumors, endogenous contrast does not provide adequate sensitivity for PAM detection of a small number of malignant tumor cells and their products. Exogenous tumor-specific contrast agents with strong optical absorption are needed to improve the detection sensitivity. Recently, ICG enhanced single walled nanoparticles (ICG-SWNP) have been used in PAM of U87MG tumors (Fig. 10) [76]. The ultrahigh surface-to-volume ratio of the SWNPs allowed for efficient loading of the optical dye onto the particle's surface. It was estimated that ~700 ICG molecules were loaded onto one SWNP. The ICG-SWNPs were then conjugated to cyclic Arg-Gly-Asp (RGD) peptides. The ICG-SWNP-RGD targeted to $\alpha_v\beta_3$ integrin, which was overexpressed in tumor. In vivo studies have demonstrated a high detection sensitivity of 170 pM of ICG-SWNP-RGD at 2 mm depth [92]. Because each tumor cell can attach ~$10^4$ nanoparticles and the detection volume is ~0.1 μL, as few as ~$10^3$ tumor cells are needed for PA imaging.

### 7.4. PAM sensitivity of other derived parameters

Originating from optical absorption, photoacoustic signals can be used to derive a number of physical, chemical and functional parameters of the absorber and its microenvironment, such as the oxygen saturation of hemoglobin [118,122,123], blood flow speed [64,91,124–128], pH [129], nonradiative relaxation time [35] and temperature [30,31]. Since a single parameter may not be able to fully reflect the true physiological and pathological conditions, multi-parameter PAM can provide a more comprehensive understanding, thus benefiting the diagnosis, staging and treatment of diseases. Here, a few representative parameters are discussed.

The oxygen saturation of hemoglobin ($sO_2$) is an important indicator of tissue oxygenation and viability. In particular, hypoxia is a hallmark of late-stage cancers [120] while hyperoxia is associated with early-stage cancers [130]. From fluence-compensated PAM measurements at two or more wavelengths, the relative concentrations of the two forms of hemoglobin can be quantified through spectral analysis, and thus $sO_2$ can be computed. The detection sensitivity of $sO_2$ is largely affected by spectral variations in the local fluence, owing to wavelength dependent optical absorption and scattering in the surrounding tissue. By choosing optimal optical wavelengths that minimize the condition number

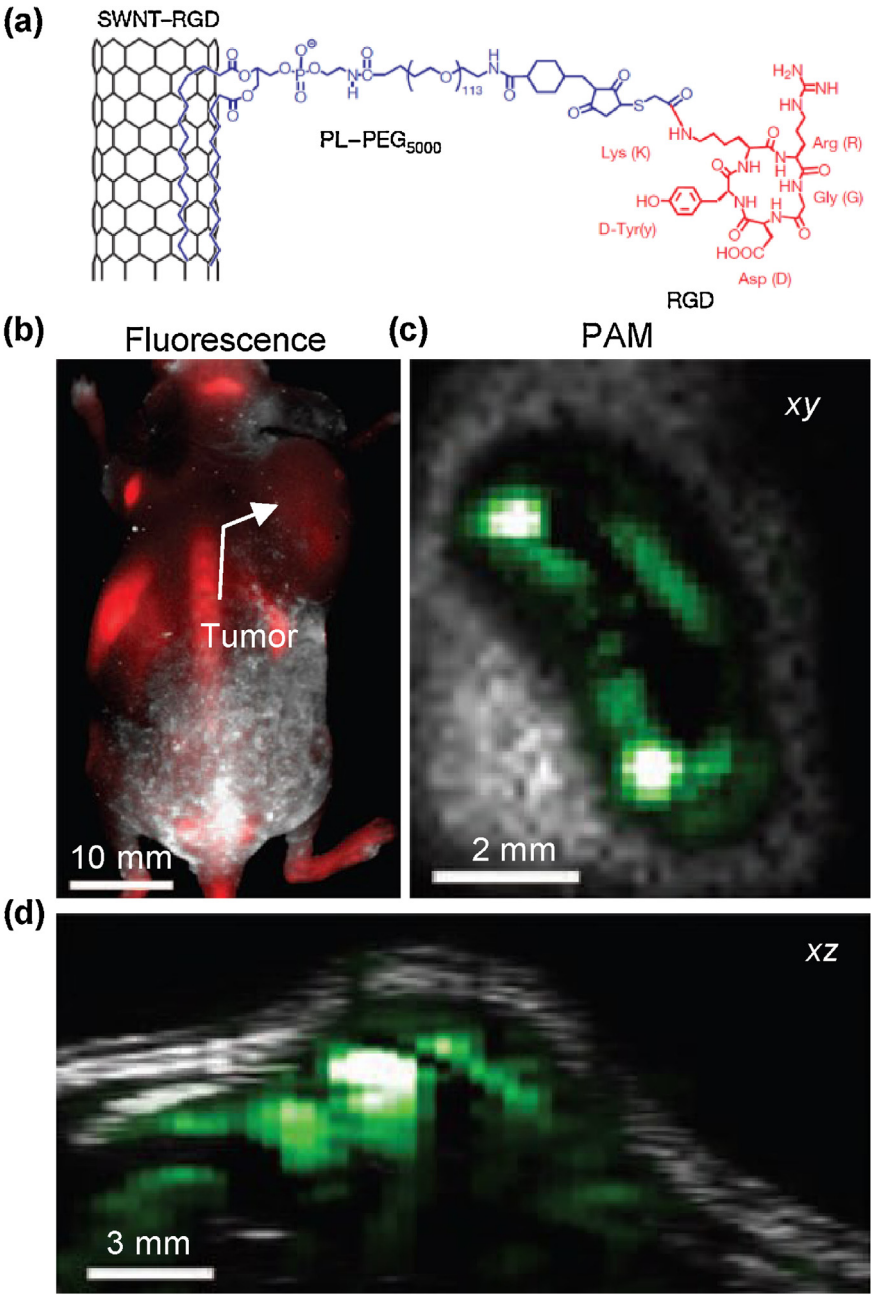


**Fig. 10.** High sensitivity photoacoustic imaging of tumor enhanced by targeted nanoparticles. (a) Chemical structure of single-walled carbon nanotubes conjugated with cyclic Arg-Gly-Asp (RGD) peptides (SWNT-RGD). (b) Fluorescence image (red) of a mouse injected with quantum dot conjugated RGD particles (QD-RGD). The white arrow indicates the tumor location. The other bright spots on the image represent different organs in which QD-RGD non-specifically accumulated. (c) Horizontal and (d) vertical slices in the 3D photoacoustic image of a mouse injected with SWNT-RGD (shown in green), superimposed on the ultrasound images (shown in gray). Reprinted with permission from [76].

of the inversion matrix and using a model-based fluence correction, an $sO_2$detection sensitivity of 1% has been demonstrated in phantom studies [131]. PAM has been used to study the temporal variations in a mouse brain in response to oxygenation alternating between hyperoxia and hypoxia [132]. A detection sensitivity of 3.6% change in oxygenation has been reported in vivo, which enables PAM monitoring of weak brain activity via hemodynamic responses. The detection sensitivity of $sO_2$ can be potentially further improved by using wavelength-independent methods based on the acoustic spectrum [118,123].

Blood flow helps keep tissue alive by distributing nutrients such as oxygen and glucose. Using the absorption contrast provided by hemoglobin, PAM can measure blood flow with a detection sensitivity one order of magnitude better than that achieved by Doppler ultrasound [64]. Recently, high-sensitivity photoacoustic flowmetry assisted by high-intensity focused ultrasound (HIFU) has been reported (Fig. 11a) [133]. This novel method employs HIFU to modulate a heating pattern in the flowing medium, followed by photoacoustic monitoring of the movement of the thermally tagged medium. Here, both the HIFU heating and photoacoustic detection can focus at depths beyond the optical diffusion limit. This method can also be applied to a continuous medium, i.e., a medium without discrete particles resolvable by photoacoustic imaging. A flow speed detection sensitivity of 0.24 mm/s has been experimentally demonstrated in a blood phantom covered by 5-mm-thick tissue.

During thermotherapy, it is necessary to monitor the local temperature distribution in the target tissues for safe deposition of

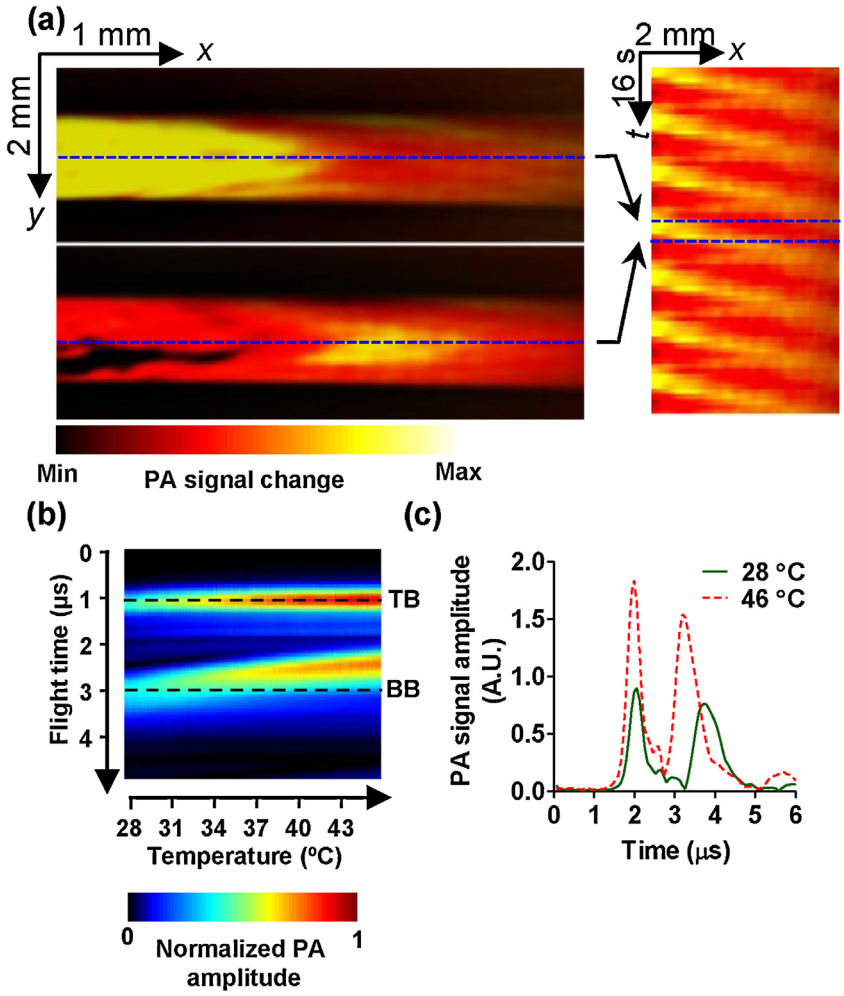


**Fig. 11.** High sensitivity photoacoustic detection of blood flow and temperature. (a) Blood flow measured by thermally tagging part of the flowing medium using a HIFU transducer and monitoring the tagged medium using photoacoustic imaging. Each horizontal line in the right figure is extracted from one photoacoustic image on the left. (b) Photoacoustic temperature measurement based on the dual-temperature dependence of the Grueneisen parameter and speed of sound. The A-line PA signals of a 3 mm blood-filled plastic tube at different temperatures are assembled and aligned at the top boundary for better visualization of the change in acoustic flight time. As the temperature increased, the PA signal amplitude increased, and the acoustic flight time between the two tube boundaries decreased. TB, top boundary; BB, bottom boundary. (c) Two example A-line signals at 28 °C and 46 °C, showing the temperature dependence of the PA signal amplitude and acoustic flight time.
Reprinted with permission from [133] for (a) and [30] for (b and c).

heat energy and efficient destruction of tumor and abnormal cells. Taking advantage of the temperature dependence of the Grueneisen parameter, PAM is capable of measuring the relative change in temperature with a high sensitivity of 0.15 °C [31]. Recently, a new photoacoustic thermometry has been developed by using the dual linear temperature dependences of the Grueneisen parameter and the speed of sound in tissue (Fig. 11b and c) [30]. Taking ratiometric measurements at two adjacent temperatures eliminates factors that are temperature irrelevant but difficult to correct for in deep tissue. Absolute temperatures of blood-filled tubes embedded ~9 mm deep in chicken tissue were measured with a detection sensitivity of ~0.6 °C, in a clinically relevant range from 28 °C to 46 °C.

## 8. Summary

The recent progress in PAM has been greatly supported by advances in laser technology, ultrasound detection methods, signal processing, and nanotechnology. From the engineering perspective, the imaging performance of PAM has been dramatically improved in almost every aspect: spatial resolution, imaging speed, penetration depth, detection sensitivity, and functionality. From the application perspective, PAM has been used in a large number of preclinical and clinical studies in cancers, diabetes, cardiovascular disease, and neural disorders. Further, PAM systems have been actively developed for small animal imaging and human skin imaging. The fast development in PAM technology has, in turn, triggered growing contributions from chemistry and nanotechnology, where a multitude of novel contrast agents have been developed, from targeted nanoparticles and organic dyes to genetically expressed markers.

With high detection sensitivity, novel PAM systems utilizing pulsed excitations and wideband ultrasonic transducers have great potential for detecting small tissue structures, such as early stage cancer, and weak physiological processes, such as neural transmission. To achieve the ultimate detection sensitivity, all the engineering aspects of a PAM system need to be carefully optimized, for the desired imaging performance, in particular for spatial resolution and imaging depth. The excitation fluence should be controlled under the safety standard, while an optimal wavelength should be chosen for maximum PA signal allowed by the targeted imaging depth. At high excitation intensity, the nonlinear PA effects, such as absorption saturation and thermal nonlinearity, need to be considered. While excitation energy delivery is not a concern for OR-PAM, optimal beam diameters and incident angles exist for dark-field AR-PAM, depending on the

targeted imaging depth. The pulse width needs to be selected to match the detection bandwidth. Wideband ultrasound transducers should be selected with an optimal piezoelectric material, central frequency and bandwidth matching the desired penetration or spatial resolution. While piezoceramic transducers are most sensitive in the frequency range below 20 MHz, lithium niobate/quartz transducers can cover the frequency range from 30 MHz to 200 MHz. Recently, novel composite piezoelectric materials have been used for high frequency ultrasonic transducers (>50 MHz)[86,134]. The combination of the optical excitation and acoustic detection also needs to be optimized, in particular for OR-PAM. While more design considerations are given to optimizing the light delivery in OR-PAM, maximizing the acoustic detection is more important in AR-PAM. Further improving the detection sensitivity of PAM relies on advances in both engineering and chemistry. In engineering, the most important factor is the development of ultrasonic transducers with high piezoelectric efficiency and low acoustic impedance, a process which includes the optimal choice of piezoelectric material, ultrasonic detection bandwidth and the backing/damping material. In chemistry, the most important factor is to develop novel contrast agents with high optical absorption and strong affinity for the targeted sites.

## Conflict of interest

The authors declare that there are no conflicts of interest.

## Acknowledgements

The authors appreciate Prof. James Ballard's close reading of the manuscript. We thank Lidai Wang and Konstantin Maslov for helpful discussions. This work was sponsored by NIH grants DP1 EB016986 (NIH Director's Pioneer Award), R01 CA186567 (NIH Director's Transformative Research Award), R01 EB016963, R01 CA134539, R01 EB010049, R01 CA157277, and R01 CA159959. L. V. Wang has a financial interest in Endra, Inc., and Microphotoacoustics, Inc., which, however, did not support this work.

## References

[1] Yang JM, Favazza C, Chen RM, Yao JJ, Cai X, Maslov K, et al. Simultaneous functional photoacoustic and ultrasonic endoscopy of internal organs in vivo. Nat Med 2012;18(8):1298–303.
[2] Kim C, Favazza C, Wang LHV. In vivo photoacoustic tomography of chemicals: high-resolution functional and molecular optical imaging at new depths. Chem Rev 2010;110(5):2756–82.
[3] Yao J, Wang LV. Photoacoustic tomography: fundamentals, advances and prospects. Contrast Media Mol Imaging 2011;6(5):332–45.
[4] Wang LV, Wu H-i. Biomedical optics: principles and imaging. Hoboken, NJ: Wiley-Interscience; 2007. xiv, 362.
[5] Wang LHV, Hu S. Photoacoustic tomography: in vivo imaging from organelles to organs. Science 2012;335(6075):1458–62.
[6] Kuchment P, Kunyansky L. Mathematics of photoacoustic and thermoacoustic tomography. In: Imaging O, Scherzer, editors. Handbook of mathematical methods. New York, NY u.a: Springer; 2011. p. 817–66.
[7] Xu MH, Wang LHV. Universal back-projection algorithm for photoacoustic computed tomography. Phys Rev E 2005;71(1):016706.
[8] Xu Y, Wang LHV. Time reversal and its application to tomography with diffracting sources. Phys Rev Lett 2004;92(3):033902.
[9] Beard P. Biomedical photoacoustic imaging. Interface Focus 2011;1(4):602–31.
[10] Yao JJ, Wang LHV. Photoacoustic microscopy. Laser Photon Rev 2013;7(5):758–78.
[11] Maslov K, Zhang HF, Hu S, Wang LV. Optical-resolution photoacoustic microscopy for in vivo imaging of single capillaries. Opt Lett 2008;33(9):929–31.
[12] Zhang HF, Maslov K, Stoica G, Wang LHV. Functional photoacoustic microscopy for high-resolution and noninvasive in vivo imaging. Nat Biotechnol 2006;24(7):848–51.
[13] Maslov K, Stoica G, Wang LHV. In vivo dark-field reflection-mode photoacoustic microscopy. Opt Lett 2005;30(6):625–7.
[14] Esenaliev RO, Karabutov AA, Oraevsky AA. Sensitivity of laser opto-acoustic imaging in detection of small deeply embedded tumors. IEEE J Select Top Quant Electron 1999;5(4):981–8.
[15] Winkler AM, Maslov K, Wang LV. Noise-equivalent sensitivity of photoacoustics. J Biomed Opt 2013;18(9):097003.
[16] Oraevsky AA, Karabutov AA. Ultimate sensitivity of time-resolved optoacoustic detection. In: Biomedical optoacoustics. San Jose, CA: SPIE; 2000.
[17] Razansky D, Baeten J, Ntziachristos V. Sensitivity of molecular target detection by multispectral optoacoustic tomography (MSOT). Med Phys 2009;36(3):939–45.
[18] Frangioni JV. New technologies for human cancer imaging. J Clin Oncol 2008;26(24):4012–21.
[19] Wang LV. Tutorial on photoacoustic microscopy and computed tomography. IEEE J Select Top Quant Electron 2008;14(1):171–9.
[20] Wang LV. Multiscale photoacoustic microscopy and computed tomography. Nat Photonics 2009;3(9):503–9.
[21] Petschke A, La Riviere PJ. Comparison of intensity-modulated continuous-wave lasers with a chirped modulation frequency to pulsed lasers for photoacoustic imaging applications. Biomed Opt Exp 2010;1(4):1188–95.
[22] Maslov K, Wang LV. Photoacoustic imaging of biological tissue with intensity-modulated continuous-wave laser. J Biomed Opt 2008;13(2):024006.
[23] Fang H, Maslov K, Wang LV. Photoacoustic Doppler effect from flowing small light-absorbing particles. Phys Rev Lett 2007;99(18):184501.
[24] Fang H, Maslov K, Wang LV. Photoacoustic Doppler flow measurement in optically scattering media. Appl Phys Lett 2007;91(26):264103.
[25] Laser Institute of America, American National Standard for Safe Use of Lasers Standard Z136.1-2007.
[26] Yang XM, Stein EW, Ashkenazi S, Wang LHV. Nanoparticles for photoacoustic imaging. Wiley Interdiscip Rev Nanomed Nanobiotechnol 2009;1(4):360–8.
[27] Sivaramakrishnan M, Maslov K, Zhang HF, Stoica G, Wang LV. Limitations of quantitative photoacoustic measurements of blood oxygenation in small vessels. Phys Med Biol 2007;52(5):1349–61.
[28] Wang J, Liu T, Jiao SL, Chen RM, Zhou QF, Shung KK, et al. Saturation effect in functional photoacoustic imaging. J Biomed Opt 2010;15(2):021317.
[29] Wang Y, Wang LV. Forster resonance energy transfer photoacoustic microscopy. J Biomed Opt 2012;17(8):086007.
[30] Yao J, Ke H, Tai S, Zhou Y, Wang LV. Absolute photoacoustic thermometry in deep tissue. Opt Lett 2013;38(24):5228–31.
[31] Pramanik M, Wang LV. Thermoacoustic and photoacoustic sensing of temperature. J Biomed Opt 2009;14(5):054024.
[32] Calasso IG, Craig W, Diebold GJ. Photoacoustic point source. Phys Rev Lett 2001;86(16):3550–3.
[33] Hopt A, Neher E. Highly nonlinear photodamage in two-photon fluorescence microscopy. Biophys J 2001;80(4):2029–36.
[34] Danielli A, Favazza CP, Maslov K, Wang LHV. Single-wavelength functional photoacoustic microscopy in biological tissue. Opt Lett 2011;36(5):769–71.
[35] Danielli A, Favazza CP, Maslov K, Wang LV. Picosecond absorption relaxation measured with nanosecond laser photoacoustics. Appl Phys Lett 2010;97(16):163701.
[36] Sonden A, Svensson B, Roman N, Ostmark H, Brismar B, Palmblad J, et al. Laser-induced shock wave endothelial cell injury. Lasers Surg Med 2000;26(4):364–75.
[37] Bost W, Stracke F, Weiss EC, Narasimhan S, Kolios MC, Lemor R. High frequency optoacoustic microscopy. Conf Proc IEEE Eng Med Biol Soc 2009;2009:5883–6.
[38] Cobbold RSC. Foundations of biomedical ultrasound. Oxford; New York: Oxford University Press; 2007. xix, 802.
[39] Liu T, Wang J, Petrov GI, Yakovlev VV, Zhang HF. Photoacoustic generation by multiple picosecond pulse excitation. Med Phys 2010;37(4):1518–21.
[40] Zhang C, Maslov K, Yao JJ, Wang LHV. In vivo photoacoustic microscopy with 7.6-mu m axial resolution using a commercial 125-MHz ultrasonic transducer. J Biomed Opt 2012;17(11):116016.
[41] Zhang C, Maslov K, Wang LHV. Subwavelength-resolution label-free photoacoustic microscopy of optical absorption in vivo. Opt Lett 2010;35(19):3195–7.
[42] Li M, Oh J-T, Xie X, Ku G, Wang W, Li C, et al. Simultaneous molecular and hypoxia imaging of brain tumors in vivo using spectroscopic photoacoustic tomography. Proc IEEE 2008;96(3):481–9.
[43] Xing W, Wang L, Maslov K, Wang LV. Integrated optical- and acoustic-resolution photoacoustic microscopy based on an optical fiber bundle. Opt Lett 2013;38(1):52–4.
[44] Estrada H, Turner J, Kneipp M, Razansky D. Real-time optoacoustic brain microscopy with hybrid optical and acoustic resolution. Laser Phys Lett 2014;11(4):045601.
[45] Xie ZX, Wang LHV, Zhang HF. Optical fluence distribution study in tissue in dark-field confocal photoacoustic microscopy using a modified Monte Carlo convolution method. Appl Opt 2009;48(17):3204–11.
[46] Wang LD, Maslov K, Xing WX, Garcia-Uribe A, Wang LHV. Video-rate functional photoacoustic microscopy at depths. J Biomed Opt 2012;17(10):106007.
[47] Favazza CP, Guo Z, Maslov K, Wang LV. Optimal oblique light illumination for photoacoustic microscopy beyond the diffusion limit. In: Photons plus ultrasound: imaging and sensing 2011. San Francisco, CA, USA: SPIE; 2011.
[48] Hu S, Maslov K, Wang LV. Second-generation optical-resolution photoacoustic microscopy with improved sensitivity and speed. Opt Lett 2011;36(7):1134–6.
[49] Wang LD, Maslov K, Yao JJ, Rao B, Wang LHV. Fast voice-coil scanning optical-resolution photoacoustic microscopy. Opt Lett 2011;36(2):139–41.

[50] Park J, Cummins TM, Harrison M, Lee J, Zhou QF, Lien CL, et al. High frequency photoacoustic imaging for in vivo visualizing blood flow of zebrafish heart. Opt Express 2013;21(12):14636–42.
[51] Ma R, Sontges S, Shoham S, Ntziachristos V, Razansky D. Fast scanning coaxial optoacoustic microscopy. Biomed Opt Exp 2012;3(7):1724–31.
[52] Lin Z, Lin C, Lu X, Ye R, Huang Y. Study of photoacoustic imaging based on all-optical detection. In: Photons plus ultrasound: imaging and sensing 2008. San Francisco, CA, USA: SPIE; 2008.
[53] Chen SL, Huang SW, Ling T, Ashkenazi S, Guo LJ. Polymer microring resonators for high-sensitivity and wideband photoacoustic imaging. IEEE Trans Ultrasonics Ferroelectr Frequency Control 2009;56(11):2482–91.
[54] Rosenthal A, Kellnberger S, Bozhko D, Chekkoury A, Omar M, Razansky D, et al. Sensitive interferometric detection of ultrasound for minimally invasive clinical imaging applications. Laser Photon Rev 2014. http://dx.doi.org/10.1002/lpor.201300204.
[55] Chen S-L, Xie Z, Guo LJ, Wang X. A fiber-optic system for dual-modality photoacoustic microscopy and confocal fluorescence microscopy using miniature components. Photoacoustics 2013;1(2):30–5.
[56] Li H, Dong B, Zhang Z, Zhang HF, Sun C. A transparent broadband ultrasonic detector based on an optical micro-ring resonator for photoacoustic microscopy. Sci Rep 2014;4:4496.
[57] Zhang EZ, Beard PC. A miniature all-optical photoacoustic imaging probe. In: Photons plus ultrasound: imaging and sensing 2011. San Francisco, CA, USA: SPIE; 2011.
[58] Zhang EZ, Laufer J, Povazay B, Alex A, Hofer B, Drexler W, et al. Multimodal simultaneous photoacoustic tomography, optical resolution microscopy, and OCT system. In: Photons plus ultrasound: imaging and sensing 2010. San Francisco, CA, USA: SPIE; 2010.
[59] Zhang E, Laufer J, Beard P. Backward-mode multiwavelength photoacoustic scanner using a planar Fabry-Perot polymer film ultrasound sensor for high-resolution three-dimensional imaging of biological tissues. Appl Opt 2008;47(4):561–77.
[60] Zhang C, Cheng Y-J, Chen J, Wickline S, Wang LV. Label-free photoacoustic microscopy of myocardial sheet architecture. J Biomed Opt 2012;17(6):060506.
[61] Zhang C, Zhang YS, Yao DK, Xia YN, Wang LHV. Label-free photoacoustic microscopy of cytochromes. J Biomed Opt 2013;18(2):020504.
[62] Zhang C, Masiov K, Hu S, Chen RM, Zhou QF, Shung KK, et al. Reflection-mode submicron-resolution in vivo photoacoustic microscopy. J Biomed Opt 2012;17(2):020501.
[63] Wang H, Yang XQ, Liu YY, Jiang BW, Luo QM. Reflection-mode optical-resolution photoacoustic microscopy based on a reflective objective. Opt Express 2013;21(20):24210–18.
[64] Yao D, Maslov K, Shung KK, Zhou Q, Wang LV. In vivo label-free photoacoustic microscopy of cell nuclei by excitation of DNA and RNA. Opt Lett 2010;35(24):4139–41.
[65] Wang LD, Maslov K, Wang LHV. Single-cell label-free photoacoustic flowoxigraphy in vivo. Proc Natl Acad Sci U S A 2013;110(15):5759–64.
[66] Shelton RL, Applegate BE. Off-axis photoacoustic microscopy. IEEE Trans Biomed Eng 2010;57(8):1835–8.
[67] Yao DK, Chen RM, Maslov K, Zhou QF, Wang LV. Optimal ultraviolet wavelength for in vivo photoacoustic imaging of cell nuclei. J Biomed Opt 2012;17(5):056004.
[68] Zhang C, Zhang YS, Yao DK, Xia YN, Wang LHV. Label-free photoacoustic microscopy of cytochromes. J Biomed Opt 2013;18(2):20504.
[69] Zhou Y, Zhang C, Yao DK, Wang LV. Photoacoustic microscopy of bilirubin in tissue phantoms. J Biomed Opt 2012;17(12):126019.
[70] Staley J, Grogan P, Samadi AK, Cui H, Cohen MS, Yang X. Growth of melanoma brain tumors monitored by photoacoustic microscopy. J Biomed Opt 2010;15(4):040510.
[71] Wang HW, Chai N, Wang P, Hu S, Dou W, Umulis D, et al. Label-free bond-selective imaging by listening to vibrationally excited molecules. Phys Rev Lett 2011;106(23):238106.
[72] Yakovlev VV, Zhang HF, Noojin GD, Denton ML, Thomas RJ, Scully MO. Stimulated Raman photoacoustic imaging. Proc Natl Acad Sci USA 2010;107(47):20335–39.
[73] Xu Z, Li CH, Wang LV. Photoacoustic tomography of water in phantoms and tissue. J Biomed Opt 2010;15(3):036019.
[74] MacKenzie HA, Ashton HS, Spiers S, Shen Y, Freeborn SE, Hannigan J, et al. Advances in photoacoustic noninvasive glucose testing. Clin Chem 1999;45(12):1587–95.
[75] Luke GP, Yeager D, Emelianov SY. Biomedical applications of photoacoustic imaging with exogenous contrast agents. Ann Biomed Eng 2012;40(2):422–37.
[76] De La Zerda A, Zavaleta C, Keren S, Vaithilingam S, Bodapati S, Liu Z, et al. Carbon nanotubes as photoacoustic molecular imaging agents in living mice. Nat Nanotechnol 2008;3(9):557–62.
[77] Kim C, Cho EC, Chen JY, Song KH, Au L, Favazza C, et al. In vivo molecular photoacoustic tomography of melanomas targeted by bioconjugated gold nanocages. ACS Nano 2010;4(8):4559–64.
[78] Galanzha EI, Shashkov EV, Kelly T, Kim JW, Yang LL, Zharov VP. In vivo magnetic enrichment and multiplex photoacoustic detection of circulating tumour cells. Nat Nanotechnol 2009;4(12):855–60.
[79] Copland JA, Eghtedari M, Popov VL, Kotov N, Mamedova N, Motamedi M, et al. Bioconjugated gold nanoparticles as a molecular based contrast agent: implications for imaging of deep tumors using optoacoustic tomography. Mol Imaging Biol 2004;6(5):341–9.
[80] Eghtedari M, Copland JA, Kotov NA, Oraevsky AA, Motamedi M. Optoacoustic imaging of nanoparticle labeled breast cancer cells: a molecular based approach for imaging of deep tumors. Lasers Surg Med 2004;S16:52.
[81] Yang XM, Skrabalak SE, Li ZY, Xia YN, Wang LHV. Photoacoustic tomography of a rat cerebral cortex in vivo with au nanocages as an optical contrast agent. Nano Lett 2007;7(12):3798–802.
[82] Pan DPJ, Pramanik M, Senpan A, Ghosh S, Wickline SA, Wang LV, et al. Near infrared photoacoustic detection of sentinel lymph nodes with gold nanobeacons. Biomaterials 2010;31(14):4088–93.
[83] Song KH, Kim CH, Cobley CM, Xia YN, Wang LV. Near-infrared gold nanocages as a new class of tracers for photoacoustic sentinel lymph node mapping on a rat model. Nano Lett 2009;9(1):183–8.
[84] Pan DPJ, Cai X, Yalaz C, Senpan A, Omanakuttan K, Wickline SA, et al. Photoacoustic sentinel lymph node imaging with self-assembled copper neodecanoate nanoparticles. ACS Nano 2012;6(2):1260–7.
[85] Rao B, Maslov K, Danielli A, Chen R, Shung KK, Zhou Q, et al. Real-time four-dimensional optical-resolution photoacoustic microscopy with Au nanoparticle-assisted subdiffraction-limit resolution. Opt Lett 2011;36(7):1137–9.
[86] Zhang C, Masiov K, Hu S, Chen RM, Zhou QF, Shung KK, et al. Reflection-mode submicron-resolution in vivo photoacoustic microscopy. J Biomed Opt 2012;17(2).
[87] Nedosekin DA, Galanzha EI, Dervishi E, Biris AS, Zharov VP. Super-resolution nonlinear photothermal microscopy. Small 2014;10(I):135–42.
[88] Oladipupo S, Hu S, Kovalski J, Yao JJ, Santeford A, Sohn RE, et al. VEGF is essential for hypoxia-inducible factor-mediated neovascularization but dispensable for endothelial sprouting. Proc Natl Acad Sci U S A 2011;108(32):13264–69.
[89] Oladipupo SS, Hu S, Santeford AC, Yao JJ, Kovalski JR, Shohet RV, et al. Conditional HIF-1 induction produces multistage neovascularization with stage-specific sensitivity to VEGFR inhibitors and myeloid cell independence. Blood 2011;117(15):4142–53.
[90] Bitton R, Zemp R, Yen J, Wang LV, Shung KK. A 3-D high-frequency array based 16 channel photoacoustic microscopy system for in vivo micro-vascular imaging. IEEE Trans Med Imaging 2009;28(8):1190–7.
[91] Chen SL, Ling T, Huang SW, Won Baac H, Guo LJ. Photoacoustic correlation spectroscopy and its application to low-speed flow measurement. Opt Lett 2010;35(8):1200–2.
[92] de la Zerda A, Liu ZA, Bodapati S, Teed R, Vaithilingam S, Khuri-Yakub BT, et al. Ultrahigh sensitivity carbon nanotube agents for photoacoustic molecular imaging in living mice. Nano Lett 2010;10(6):2168–72.
[93] Li L, Zhang HF, Zemp RJ, Maslov K, Wang L. Simultaneous imaging of a lacZ-marked tumor and microvasculature morphology in vivo by dual-wavelength photoacoustic microscopy. J Innov Opt Health Sci 2008;1(2):207–15.
[94] Li ML, Wang JC, Schwartz JA, Gill-Sharp KL, Stoica G, Wang LHV. In-vivo photoacoustic microscopy of nanoshell extravasation from solid tumor vasculature. J Biomed Opt 2009;14(1):010507.
[95] Olafsson R, Bauer DR, Montilla LG, Witte RS. Real-time, contrast enhanced photoacoustic imaging of cancer in a mouse window chamber. Opt Express 2010;18(18):18625–32.
[96] Hu S, Maslov K, Tsytsarev V, Wang LV. Functional transcranial brain imaging by optical-resolution photoacoustic microscopy. J Biomed Opt 2009;14(4):040503.
[97] Wang XD, Ku G, Wegiel MA, Bornhop DJ, Stoica G, Wang LHV. Noninvasive photoacoustic angiography of animal brains in vivo with near-infrared light and an optical contrast agent. Opt Lett 2004;29(7):730–2.
[98] Liao LD, Li ML, Lai HY, Shih YYI, Lo YC, Tsang SN, et al. Imaging brain hemodynamic changes during rat forepaw electrical stimulation using functional photoacoustic microscopy. Neuroimage 2010;52(2):562–70.
[99] Tsytsarev V, Hu S, Yao J, Maslov K, Barbour DL, Wang LV. Photoacoustic microscopy of microvascular responses to cortical electrical stimulation. J Biomed Opt 2011;16(7):076002.
[100] Subach FV, Zhang LJ, Gadella TWJ, Gurskaya NG, Lukyanov KA, Verkhusha VV. Red fluorescent protein with reversibly photoswitchable absorbance for photochromic FRET. Chem Biol 2010;17(7):745–55.
[101] Jiao SL, Jiang MS, Hu JM, Fawzi A, Zhou QF, Shung KK, et al. Photoacoustic ophthalmoscopy for in vivo retinal imaging. Opt Express 2010;18(4):3967–72.
[102] Xie X, Jiao SL, Zhang HF, Puliafito CA. Laser-scanning optical-resolution photoacoustic microscopy. Opt Lett 2009;34(12):1771–3.
[103] Silverman RH, Kong F, Chen YC, Lloyd HO, Kim HH, Cannata JM, et al. High-resolution photoacoustic imaging of ocular tissues. Ultrasound Med Biol 2010;36(5):733–42.
[104] Song W, Wei Q, Liu T, Kuai D, Burke JM, Jiao S, et al. Integrating photoacoustic ophthalmoscopy with scanning laser ophthalmoscopy, optical coherence tomography, and fluorescein angiography for a multimodal retinal imaging platform. J Biomed Opt 2012;17(6):061206–61207.
[105] Zhang HF, Maslov K, Li ML, Stoica G, Wang LHV. In vivo volumetric imaging of subcutaneous microvasculature by photoacoustic microscopy. Opt Express 2006;14(20):9317–23.
[106] Favazza C, Maslov K, Cornelius L, Wang LV. In vivo functional human imaging using photoacoustic microscopy: response to ischemic and thermal stimuli. In: Photons plus ultrasound: imaging and sensing, 2010. San Francisco, CA, USA: SPIE; 2010.

[107] Favazza CP, Cornelius LA, Wang LHV. In vivo functional photoacoustic microscopy of cutaneous microvasculature in human skin. J Biomed Opt 2011;16(2):026004.
[108] Favazza C, Jassim O, Wang LV, Cornelius L. In vivo photoacoustic microscopy of human skin. J Invest Dermatol 2010;130:S145.
[109] Song LA, Maslov K, Shung KK, Wang LHV. Ultrasound-array-based real-time photoacoustic microscopy of human pulsatile dynamics in vivo. J Biomed Opt 2010;15(2):021303.
[110] Yang J-M, Chen R, Favazza C, Yao J, Zhou Q, Shung KK, et al. A 2.5-mm outer diameter photoacoustic endoscopic mini-probe based on a highly sensitive PMN-PT ultrasonic transducer. In: Photons plus ultrasound: imaging and sensing, 2012. San Francisco, CA, USA: SPIE; 2012.
[111] Yang J-M, Favazza C, Chen R, Yao J, Cai X, Maslov K, et al. Toward dual-wavelength functional photoacoustic endoscopy: laser and peripheral optical systems development. In: Photons plus ultrasound: imaging and sensing, 2012. San Francisco, CA, USA: SPIE; 2012.
[112] Yao J, Maslov KI, Puckett ER, Rowland KJ, Warner BW, Wang LV. Double-illumination photoacoustic microscopy. Opt Lett 2012;37(4):659–61.
[113] Yao J, Rowland KJ, Wang L, Maslov KI, Warner BW, Wang LV. Double-illumination photoacoustic microscopy of intestinal hemodynamics following massive small bowel resection. In: Photons plus ultrasound: imaging and sensing, 2012. San Francisco, CA, USA: SPIE; 2012.
[114] Rowland KJ, Yao JJ, Wang LD, Erwin CR, Maslov KI, Wang LHV, et al. Immediate alterations in intestinal oxygen saturation and blood flow after massive small bowel resection as measured by photoacoustic microscopy. J Pediatr Surg 2012;47(6):1143–9.
[115] Taruttis A, Herzog E, Razansky D, Ntziachristos V. Real-time imaging of cardiovascular dynamics and circulating gold nanorods with multispectral optoacoustic tomography. Opt Express 2010;18(19):19592–602.
[116] Wang B, Su JL, Karpiouk AB, Sokolov KV, Smalling RW, Emelianov SY. Intravascular photoacoustic imaging. IEEE J Select Top Quant Electron 2010;16(3):588–99.
[117] Zemp RJ, Song L, Bitton R, Shung KK, Wang LV. Realtime photoacoustic microscopy of murine cardiovascular dynamics. Opt Express 2008;16(22):18551–56.
[118] Guo ZJ, Hu S, Wang LHV. Calibration-free absolute quantification of optical absorption coefficients using acoustic spectra in 3D photoacoustic microscopy of biological tissue. Opt Lett 2010;35(12):2067–9.
[119] Hu S, Wang LV. Photoacoustic imaging and characterization of the microvasculature. J Biomed Opt 2010;15(1):011101.
[120] Hanahan D, Weinberg RA. Hallmarks of cancer: the next generation. Cell 2011;144(5):646–74.
[121] Galanzha EI, Shashkov EV, Spring PM, Suen JY, Zharov VP. In vivo, noninvasive, label-free detection and eradication of circulating metastatic melanoma cells using two-color photoacoustic flow cytometry with a diode laser. Cancer Res 2009;69(20):7926–34.
[122] Zhang HF, Maslov K, Sivaramakrishnan M, Stoica G, Wang LHV. Imaging of hemoglobin oxygen saturation variations in single vessels in vivo using photoacoustic microscopy. Appl Phys Lett 2007;90(5):053901.
[123] Guo Z, Favazza C, Garcia-Uribe A, Wang LV. Quantitative photoacoustic microscopy of optical absorption coefficients from acoustic spectra in the optical diffusive regime. J Biomed Opt 2012;17(6):066011.
[124] Yao J, Maslov KI, Wang LV. In vivo photoacoustic tomography of total blood flow and potential imaging of cancer angiogenesis and hypermetabolism. Technol Cancer Res Treat 2012;11(4):301–7.
[125] Yao JJ, Wang LHV. Transverse flow imaging based on photoacoustic Doppler bandwidth broadening. J Biomed Opt 2010;15(2):021304.
[126] Brunker J, Beard P. Pulsed photoacoustic Doppler flowmetry using a cross correlation method. In: Photons plus ultrasound: imaging and sensing, 2010. San Francisco, CA, USA: SPIE; 2010.
[127] Sheinfeld A, Eyal A. Photoacoustic thermal diffusion flowmetry. Biomed Opt Exp 2012;3(4):800–13.
[128] Sheinfeld A, Gilead S, Eyal A. Time-resolved photoacoustic Doppler characterization of flow using pulsed excitation. In: Photons plus ultrasound: imaging and sensing, 2010. San Francisco, CA, USA: SPIE; 2010.
[129] Chatni MR, Yao JJ, Danielli A, Favazza CP, Maslov KI, Wang LHV. Functional photoacoustic microscopy of pH. J Biomed Opt 2011;16(10):100503.
[130] Yao J, Maslov KI, Zhang Y, Xia Y, Wang LV. Label-free oxygen-metabolic photoacoustic microscopy in vivo. J Biomed Opt 2011;16(7):076003.
[131] Maslov K, Zhang HF, Wang LV. Effects of wavelength-dependent fluence attenuation on the noninvasive photoacoustic imaging of hemoglobin oxygen saturation in subcutaneous vasculature in vivo. Inverse Problems 2007;23(6):S113–22.
[132] Stein EW, Maslov K, Wang LHV. Noninvasive, in vivo imaging of blood-oxygenation dynamics within the mouse brain using photoacoustic microscopy. J Biomed Opt 2009;14(2):020502.
[133] Wang L, Xia J, Yao J, Maslov KI, Wang LV. Ultrasonically encoded photoacoustic flowgraphy in biological tissue. Phys Rev Lett 2013;111(20):204301.
[134] Hsu H-S, Benjauthrit V, Zheng F, Chen R, Huang Y, Zhou Q, et al. PMN-PT–PZT composite films for high frequency ultrasonic transducer applications. Sens Actuators A Phys 2012;179:121–4.
[135] Kim C, Erpelding TN, Jankovic L, Pashley MD, Wang LHV. Deeply penetrating in vivo photoacoustic imaging using a clinical ultrasound array system. Biomed Opt Exp 2010;1(1):278–84.
[136] Song KH, Wang LV. Deep reflection-mode photoacoustic imaging of biological tissue. J Biomed Opt 2007;12(6):060503.
[137] Yao J, Wang L, Li C, Zhang C, Wang LV. Photoimprint photoacoustic microscopy for three-dimensional label-free subdiffraction imaging. Phys Rev Lett 2014;112(1):014302.
[138] Ku G, Maslov K, Li L, Wang LHV. Photoacoustic microscopy with 2-mu m transverse resolution. J Biomed Opt 2010;15(2):021302.
[139] Yao JJ, Maslov K, Hu S, Wang LHV. Evans blue dye-enhanced capillary-resolution photoacoustic microscopy in vivo. J Biomed Opt 2009;14(5):054049.
[140] Pan DP, Pramanik M, Senpan A, Yang XM, Song KH, Scott MJ, et al. Molecular photoacoustic tomography with colloidal nanobeacons. Angew Chem Int Ed 2009;48(23):4170–3.
[141] Li PC, Wang CRC, Shieh DB, Wei CW, Liao CK, Poe C, et al. In vivo photoacoustic molecular imaging with simultaneous multiple selective targeting using antibody-conjugated gold nanorods. Opt Express 2008;16(23):18605–15.
[142] Ku G, Wang LHV. Deeply penetrating photoacoustic tomography in biological tissues enhanced with an optical contrast agent. Opt Lett 2005;30(5):507–9.
[143] Filonov GS, Krumholz A, Xia J, Yao JJ, Wang LHV, Verkhusha VV. Deep-tissue photoacoustic tomography of a genetically encoded near-infrared fluorescent probe. Angew Chem Int Ed 2012;51(6):1448–51.
[144] Song KH, Stein EW, Margenthaler JA, Wang LV. Noninvasive photoacoustic identification of sentinel lymph nodes containing methylene blue in vivo in a rat model. J Biomed Opt 2008;13(5):054033.
[145] Krumholz A, VanVickle-Chavez SJ, Yao JJ, Fleming TP, Gillanders WE, Wang LHV. Photoacoustic microscopy of tyrosinase reporter gene in vivo. J Biomed Opt 2011;16(8):080503.
[146] Kim C, Qin RG, Xu JS, Wang LV, Xu R. Multifunctional microbubbles and nanobubbles for photoacoustic and ultrasound imaging. J Biomed Opt 2010;15(1):010510.

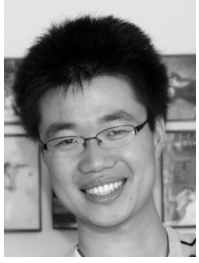

**Junjie Yao** is currently a postdoctoral research associate at Washington University in St. Louis, St. Louis, MO, under the supervision of Dr. Lihong V. Wang. His research interests are the development of novel biomedical imaging techniques including photoacoustic imaging and ultrasonic imaging.

**Lihong V. Wang** currently holds the Gene K. Beare Distinguished Professorship of Biomedical Engineering at Washington University in St. Louis. Professor Wang is a Fellow of the AIMBE (American Institute for Medical and Biological Engineering), OSA (Optical Society of America), IEEE (Institute of Electrical and Electronics Engineers), and SPIE (Society of Photo-Optical Instrumentation Engineers). He is the Editor-in-Chief of the Journal of Biomedical Optics.